



# Mechanics of thermal spallation and fracturing of dry rocks produced by surface heating

Yide Guo<sup>1,2,4</sup> · Arcady Dyskin<sup>2,4</sup> · Elena Pasternak<sup>3,4</sup> · Xibing Li<sup>1</sup> · Linqi Huang<sup>1</sup>

Received: 17 July 2023 / Accepted: 8 January 2024 / Published online: 22 February 2024  
© The Author(s), under exclusive licence to Springer-Verlag GmbH Germany, part of Springer Nature 2024

## Abstract

This paper reports the results of thermal spallation experiments on specially dried shale samples with 3 bedding orientations (0°, 45° and 90°) under 3 flame temperatures (899 °C, 1243 °C and 1559 °C) and the 3D thermal elastic finite element modelling. Under open flame heating, continuous spallation is observed with ejection of various spalls and popping sounds. After a period of spallation, tensile fractures are formed in the samples and grow perpendicular to the heating surface, except for a sample with bedding orientation of 90° under the low temperature. Increasing flame temperature promotes ejection, popping sounds and spallation rate, but reduces the spallation starting time, spallation duration, depression diameter and depression depth. The model shows that heating induces compressive stress in the surface layer and tensile stresses beneath it. The tensile stress is found to be sufficient to generate large tensile fractures. The ratio between the induced compressive and tensile stresses increases with increasing spallation depth but little affected by the flame temperature. The spallation compressive stress increases with temperature from 29 to 51% of the uniaxial compressive strength. This stress is shown to be sufficient to cause buckling of thin layers separated from the bulk of the rock. The size of the buckling layer is smaller than the size of the spallation zone leading to a mosaic pattern seen on the surface after spallation. The results are important for further understanding of the mechanism of thermal spallation of rocks as well as large scale spallation-like processes in the Earth's crust.

**Keywords** Effect of free surface · Layer buckling · Mosaic spallation · Thermal spallation · Tensile fracturing

## 1 Introduction

When rocks (or concretes) are subjected to surface heating (e.g. by a flame jet or fire), the rock surface and a thin surface layer will rapidly be heated up and undergo thermal expansion. At the same time the rest of the rock remains almost unimpacted because of the low thermal conductivity, thus limiting the expansion of the surface layer [6, 22, 24, 26, 42]. This induces compressive stresses in the surface layer and tensile stresses beneath it, Fig. 1. If the surface temperature is high enough, the compressive stresses initiate spallation produced by fractures developed from pre-existing cracks under compression and then extensively growing parallel to the surface. The resulting larger fractures separate a thin layer from the bulk of the material. The layer eventually buckles opening a new surface which starts being subjected to flame heating, Fig. 2. Then under continuous heating, the process repeats itself producing a cavity growing into the rock normal to

---

✉ Yide Guo  
yide.guo@uwa.edu.au

✉ Arcady Dyskin  
arcady.dyskin@uwa.edu.au

✉ Elena Pasternak  
elena.pasternak@uwa.edu.au

<sup>1</sup> School of Resources and Safety Engineering, Central South University, Changsha 410083, China

<sup>2</sup> Department of Civil, Environment and Mining Engineering, The University of Western Australia, Perth 6009, Australia

<sup>3</sup> Department of Mechanical Engineering, The University of Western Australia, Perth 6009, Australia

<sup>4</sup> International Space Centre, The University of Western Australia, Perth 6009, Australia

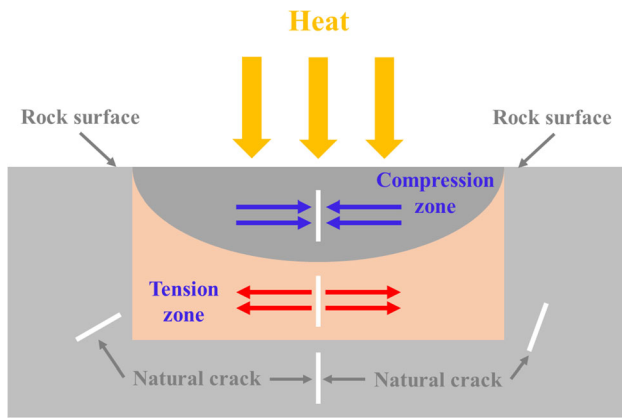


**Fig. 1** Thermal stress fields induced by surface heating (modified from Germanovich [6] and Khor and Dyskin [24])

the surface. If the magnitude of the tensile thermal stress developed beneath the compressed part of the rock reaches the tensile strength of the rock, fractures get initiated and then grow perpendicularly to the heating surface since the maximum principal direction of the tensile stress is parallel to the surface. This ends the spallation process. It should also be noted that another possible mechanism of tensile fracture formation could be the internal water evaporating under heating inducing internal pressure [15, 24, 27, 30, 49].

In the past decades, techniques based on thermal spallation have been developed primarily for rock breaking and cutting e.g. for well drilling in oil and gas extraction projects [26], drilling or extending blast holes in mining projects [22, 34, 48], predicting concrete breaking in tunnel fire [49]. Obviously thermal spallation can be a method of choice for rock breaking for outer space construction and mining, since it does not require heavy equipment [25, 45]. Continuous and intermittent thermal spallation phenomena of various rocks under open flame were widely observed in the laboratory [21, 26, 39, 42, 44].

Since the 1930s, efforts were directed towards investigating the spallation phenomena in various rocks and concretes and to classify possible mechanisms of spallation. Preston and White [32] put clay balls into hot furnace and after a certain time observed thermal spallation producing spalls in the shape of roughly circular discs of a

certain thickness. They proposed the spallation mechanism based on the growth of pre-existing cracks parallel to the free surface under compressive thermal stress. Hasenjäger [12] argued that thermal spallation of concrete samples under open fire was caused by thermal stresses and internal pressure from moisture, but so far, the dominance of the two is still disputed. Freeman et al. [5] experimentally investigated the spallability of rocks and based the spallation mechanism on the change in thermal expansion characteristics of the  $\alpha$ - $\beta$  quartz transition at 573 °C. Thirumalai [40] compared thermal spallation processes in Sioux Quartzite, Charcoal Granite and Dresser Basalt and found that thermal spallation depended upon the thermal expansion, shear strain at failure and non-elastic characteristics of the rocks, which can inhibit thermal spallation. Rauenzahn and Tester [34] agreed with the Preston and White's [32] mechanism based on growth of pre-existing cracks parallel to free surface, and concluded that the induced thermal fractures just play a secondary role in producing spallation. Wilkinson and Tester [47] proposed a thermal spallation mechanism based on crack growth aligned with the principal directions of the compressive thermal stress field, and the competition between stacking due to thermal expansion and stress relief induced by deformation of the adjacent soft materials. Hertz and Sørensen [16] after a series of laboratory tests on concrete concluded that restraining thermal expansion can prevent the thermal spallation. Smith and Pells [38] performed flame heating on Hawkesbury sandstone, and suggested that the thermal spallation was primarily generated by steam pressure. Jansson and Boström [20] held the view that the exposure condition of concrete samples to the heating controls thermal spallation because it determines the stress distribution as well as the escape routes of pore moisture. Walsh and Lomov [43] analysed the rock microstructure effect and developed a numerical tool that can conduct explicit modelling of thermal spallation at the grain-scale. Using that tool, a conclusion was made that fluid in the micropores inside the rock played significant role in producing thermal spallation. Kendrick et al. [23] investigated the spallation erosion of granitic rock caused by chaparral wildfire and viewed the rock spallation as a behaviour where the stress related to thermal expansion

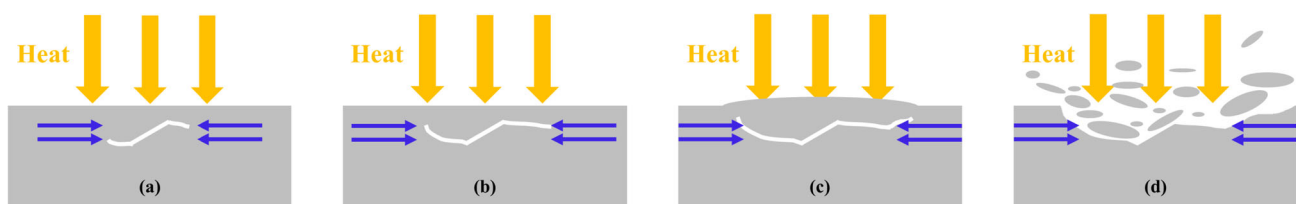


**Fig. 2** Thermal spallation: **a** initial growth stage of fracture; **b** further fracture growth under increasing compressive stress; **c** buckling layer and **d** produced spalls (modified from Khor and Dyskin [24])

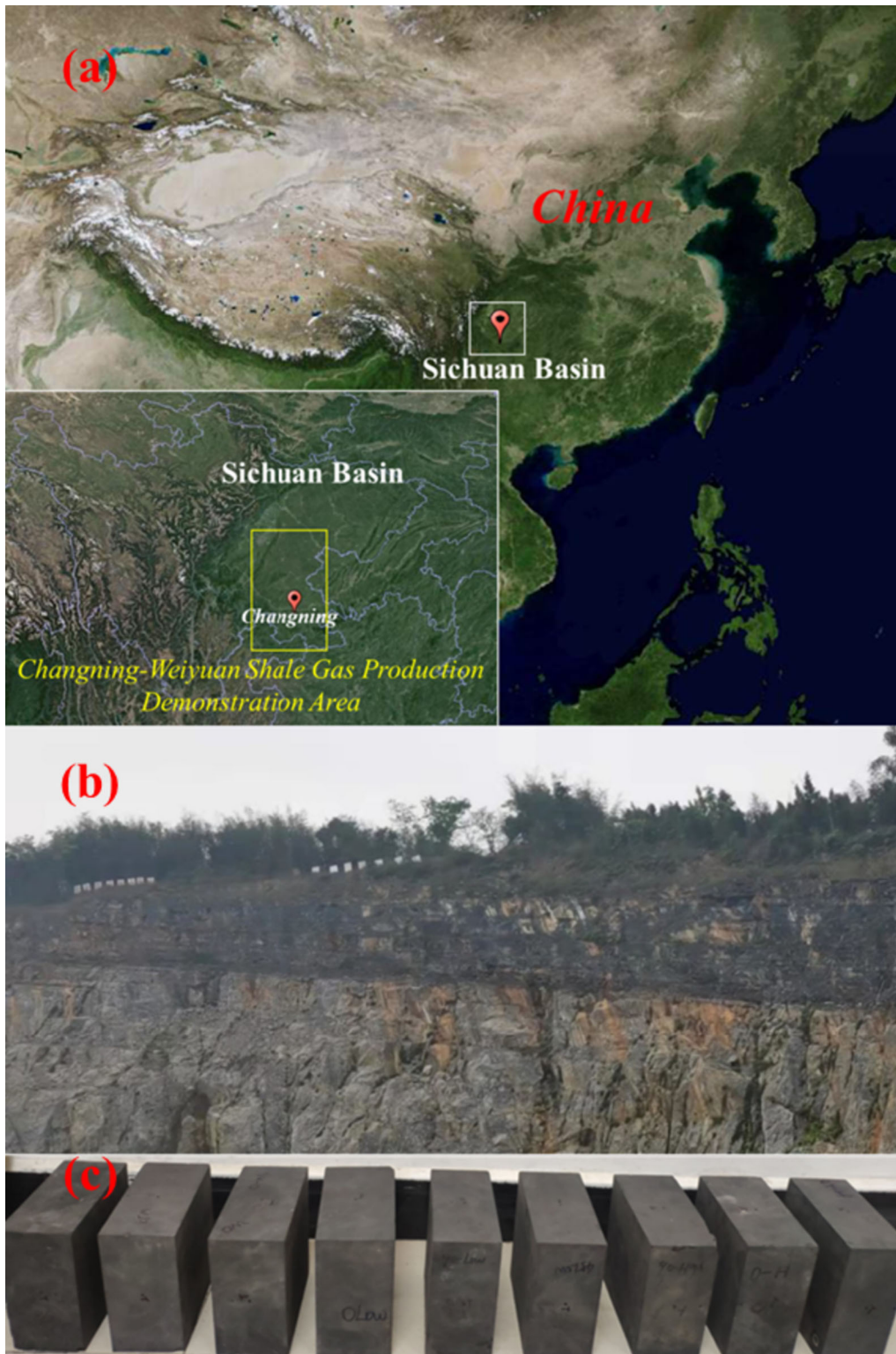


**Fig. 3** Shale samples: **a** location of national shale gas production area in Sichuan Basin; **b** the sampled outcrop; **c** the 9 dry shale samples prepared for the tests

exceeded the tensile strength of the rock. (This however contradicts the directions of principal tensile stresses which

can only produce fractures normal to the surface rather than parallel as needed for spallation.)



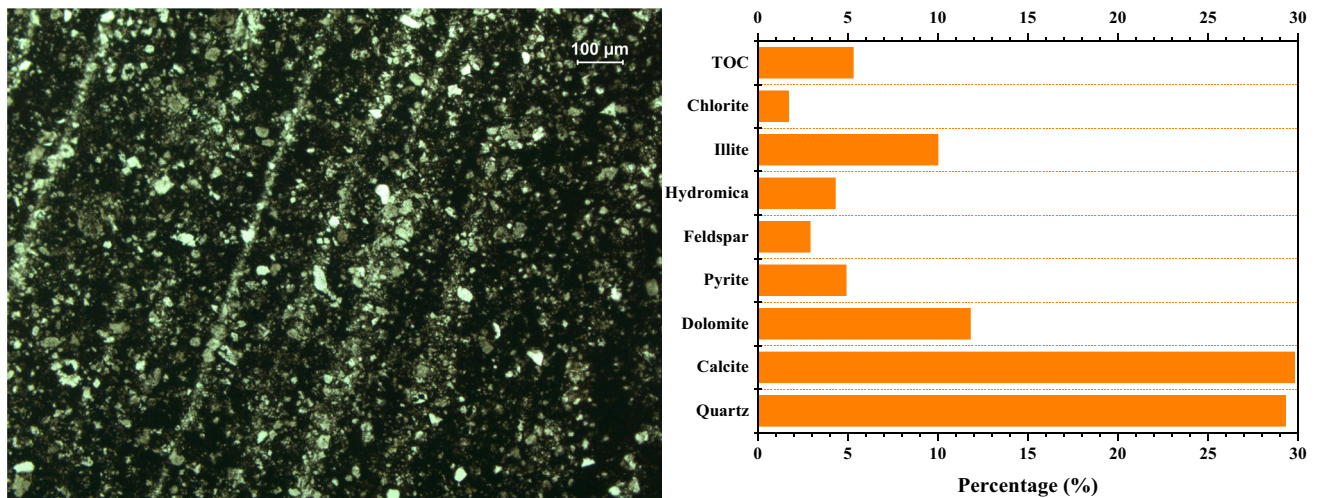


Fig. 4 Optical microscope view of microstructure and X-ray diffraction obtained composition of the Longmaxi formation shale

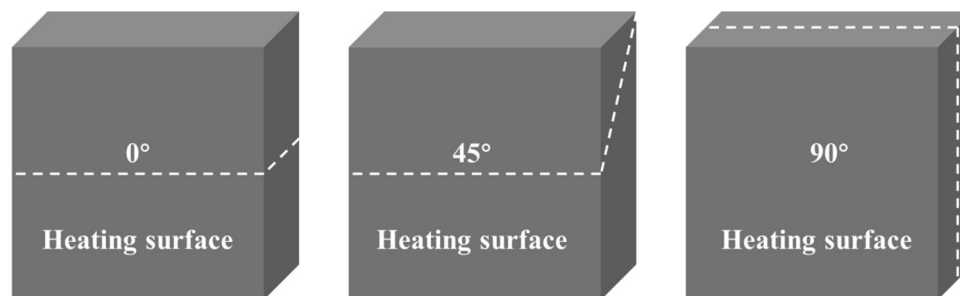


Fig. 5 Three bedding orientations of samples in the flame heating experiment

Table 1 Thermal and mechanical properties of shale samples with 3 bedding orientations [7, 9, 10]

Bedding orientation (°)	UCS <sup>a</sup> (MPa)	UTS <sup>b</sup> (MPa)	Elastic modulus (GPa)	Poisson's ratio	Specific heat (J/kg·K)	Thermal conductivity (W/m·K)	Expansion coefficient
0	121.97	5.93	22.12	0.24	850	2.14	2.32E-6
45	88.90	6.92	21.20	0.17	850	2.14	2.32E-6
90	129.99	5.10	23.60	0.23	850	2.14	2.32E-6

<sup>a</sup> Uniaxial compression strength-UCS; <sup>b</sup> Uniaxial tensile strength-UTS

There is still uncertainty as to what is the role the proposed different mechanisms play in the phenomenon of thermal spallation. Germanovich [6] devised a two-dimensional micro-mechanical model for thermal spallation induced by flame heating, and also attributed the spallation to the growth of pre-existed cracks under high compressive stress. By investigating flame heating of concrete samples, Khor and Dyskin [24] classified thermal spallation into two types, explosive and non-explosive spallation, and suggested that the thermal compressive stress as well as pressure from moisture could produce the spallation. Also,

high tensile strength was necessary for thermal spallation because it would suppress the fracture formation and splitting failure.

So far, the available experiments and numerical models cannot satisfactorily classify the spallation type and identify the spallation processes caused by only thermal stresses. Thus, further investigations are needed to clarify the mechanisms of thermal spallation and growth conditions of thermal fractures in tensile zone under the compressive surface layer. This will assist in designing and optimizing the thermal spallation-based cutting/breaking process.



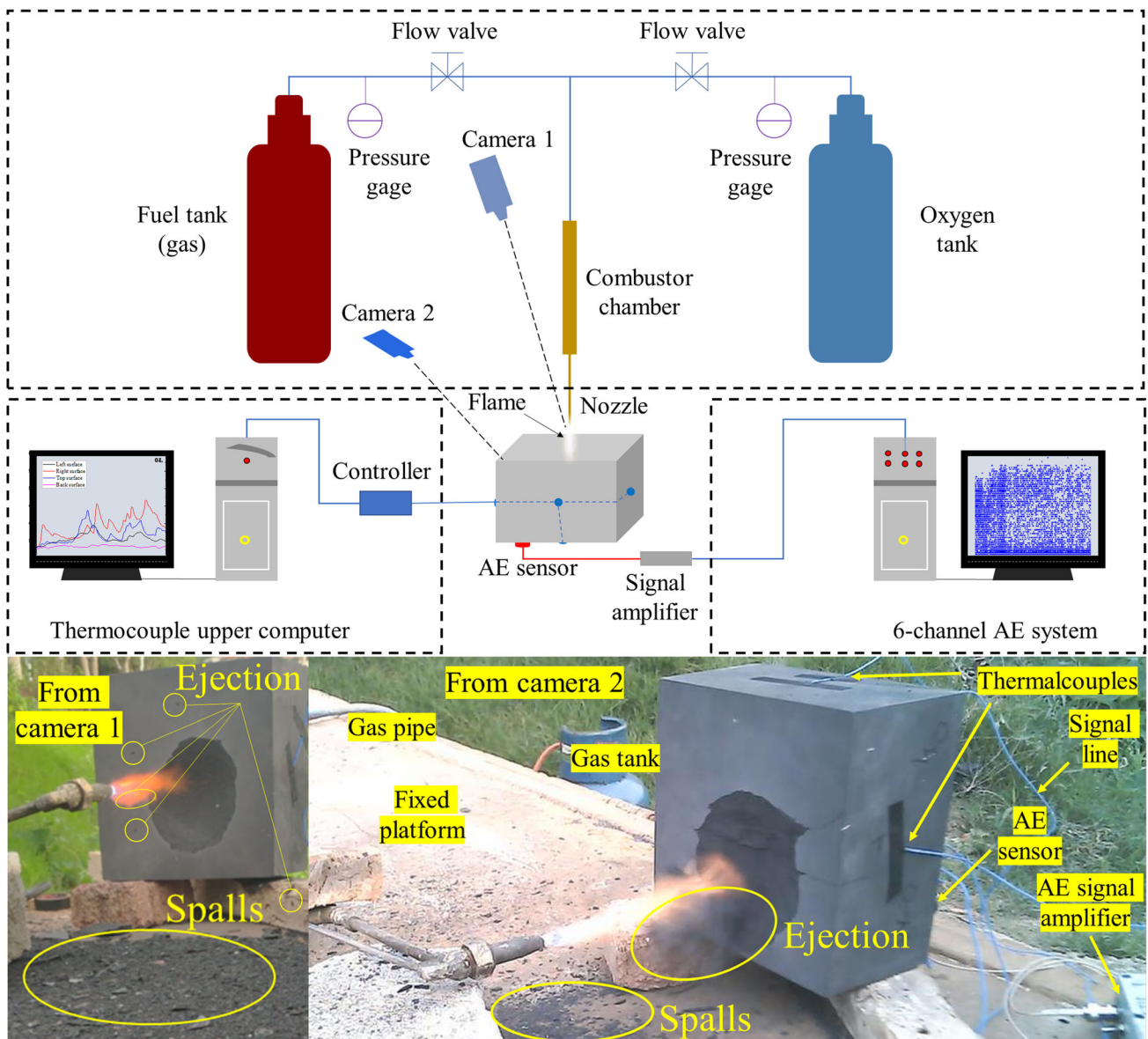


**Fig. 6** Experimental setup of flame heating and two representative scene views from cameras

Furthermore, to the best of our knowledge, there is limited research work on thermal spallation of shale, despite shale being a common geological material in many important rock engineering projects.

The present work aims at investigating thermal spallation in specially dried shale samples thus concentrating on pure thermal stress mechanism of spallation. It reports flame heating of dry Longmaxi shale samples with 3 bedding orientations under 3 flame temperatures and the corresponding 3D finite element simulations of induced thermal stresses for different continuous spallation depths (depths of the spallation depressions). The effect of flame temperature on the spallation characteristics is observed, and an analysis of the stress and temperature fields during

continuous thermal spallation of shale samples is performed to check whether the thermal fractures can solely be produced by the thermal tensile stresses in the layer situated under the compressive layer.

The paper is structured as follows. The next, Sect. 2 describes the shale samples and the testing setup and presents the experimental results. Section 3 describes the numerical model and presents the results of parametric analysis. Section 4 discusses the obtained results.

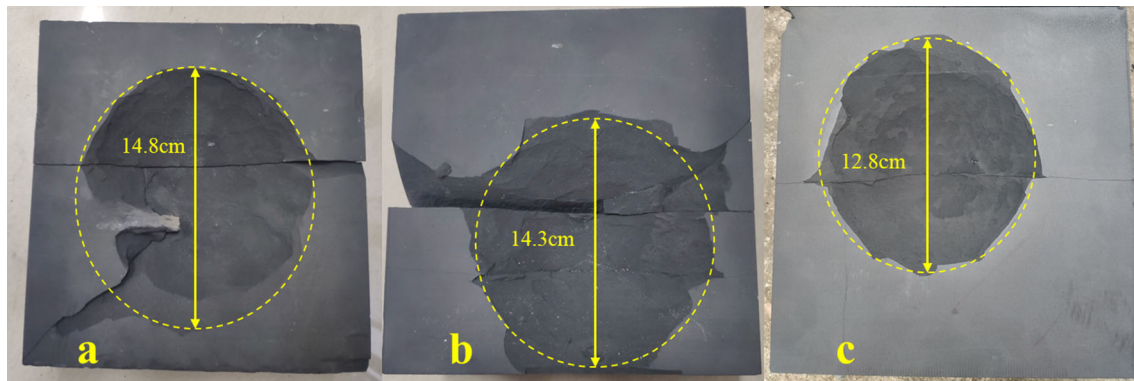


**Fig. 7** Spallation depression and the fracture in the samples with bedding orientation of  $0^\circ$  (Fig. 5): **a** low temperature-899 °C; **b** medium temperature-1243 °C; **c** high temperature-1559 °C

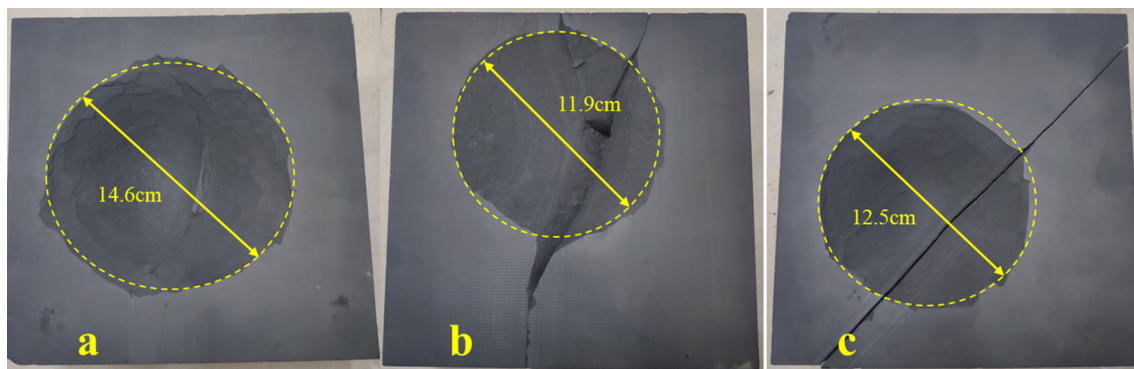


**Fig. 8** Spallation depression and the fracture in the samples with bedding orientation of  $45^\circ$  (Fig. 5): **a** low temperature-899 °C; **b** medium temperature-1243 °C; **c** high temperature-1559 °C

## 2 Experiments

### 2.1 Shale samples

The Longmaxi formation shale is found in the main areas of southwest China, especially the Sichuan Basin, Fig. 3a, and is considered to be the mother rock of the most potential shale gas reservoirs in China [8]. A large shale

block that ensured geometric integrity and lithologic consistency in an unweathered area below the ground surface was excavated near the national shale gas production site in Changning County, Sichuan Basin, to prepare the test samples, Fig. 3b. After putting this large shale block in a well-ventilated storage room for drying over 3 months, 9 dry parallelepiped samples were cut out for this experimental work with the length, width and thickness of

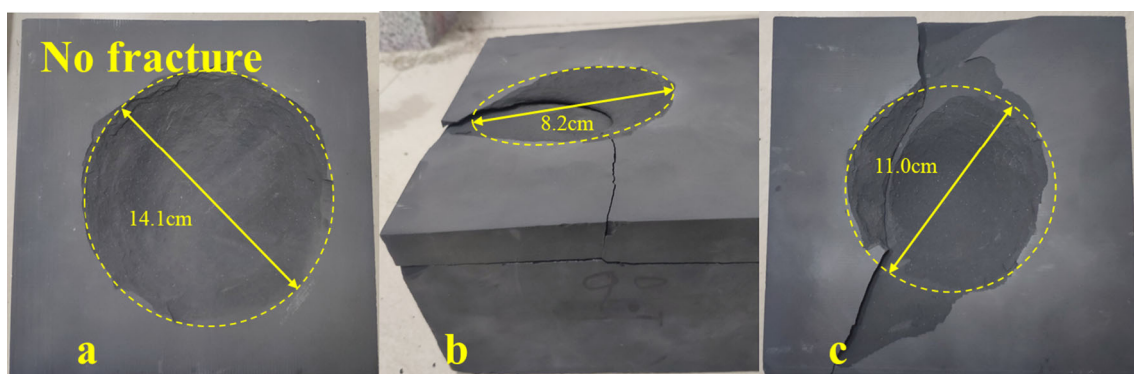


**Fig. 9** Spallation depression and the fracture in the samples with bedding orientation of  $90^\circ$  (Fig. 5): **a** low temperature-899 °C; **b** medium temperature-1243 °C; **c** high temperature-1559 °C

**Table 2** Parameters of thermal spallation of the 9 shale samples

Sample name	Flame temperatures (°C)	Spallation beginning (s)	Spallation depth (cm)	Spallation diameter (cm)	Spallation duration (s)	Spallation rate (cm/s)	Fracturing condition	Time from the start of heating to the fractures start (s)
0-L	899	3.3	3.8	14.8	149	0.0255	Tensile	43
0-M	1243	2.8	3.5	14.3	123	0.0285	Tensile	60
0-H	1559	2.1	3.2	12.8	101	0.0317	Tensile	76
45-L	899	3.2	3.7	14.6	103	0.0360	Tensile	86
45-M	1243	3.2	2.3	11.9	56	0.0411	Tensile	19
45-H	1559	2.5	3.1	12.5	73	0.0425	Tensile	10
90-L	899	3.2	3.6	14.1	158	0.0228	No fracture	–
90-M	1243	3.0	0.8	8.2	29	0.0276	Tensile	24
90-H	1559	2.3	2.7	11.0	67	0.0403	Tensile	21

**Table 3** Thickness of spalls above powder grade collected in the experiments

Bedding orientation (°)	Flame temperatures*	Spalls thickness (mm)						
		Spalls 1	Spalls 2	Spalls 3	Spalls 4	Spalls 5	Spalls 6	Average value
0	L	0.48	0.82	0.54	0.88	0.63	0.71	0.68
	M	0.71	0.67	0.59	0.61	0.66	0.54	0.63
	H	0.64	0.47	0.60	0.75	0.52	0.69	0.61
45	L	0.36	0.58	0.67	0.66	0.72	0.55	0.59
	M	0.65	0.58	0.68	0.43	0.62	0.59	0.59
	H	0.46	0.31	0.63	0.49	0.28	0.57	0.46
90	L	0.80	0.55	0.51	0.74	0.7	0.66	0.66
	M	0.59	0.56	0.67	0.77	0.53	0.75	0.65
	H	0.68	0.55	0.44	0.63	0.59	0.53	0.57

\* L-899 °C; M-1243 °C; H-1559 °C

**Table 4** Diameter of spalls above powder grade collected in the experiments

Bedding orientation (°)	Flame temperatures*	Spalls diameter (cm)						
		Spalls 1	Spalls 2	Spalls 3	Spalls 4	Spalls 5	Spalls 6	Average value
0	L	2.25	2.71	2.92	1.85	3.03	2.40	2.53
	M	1.50	1.77	2.82	2.00	1.01	1.54	1.77
	H	1.18	1.39	0.92	2.23	1.41	1.06	1.37
45	L	2.83	2.56	2.58	1.72	1.67	2.51	2.31
	M	1.33	2.19	2.07	1.89	1.82	2.07	1.90
	H	0.95	1.42	1.04	1.35	1.20	1.22	1.20
90	L	2.97	3.18	2.55	3.03	4.21	1.82	2.96
	M	1.56	1.36	1.57	2.49	1.56	2.39	1.82
	H	2.78	2.07	1.62	1.09	1.31	1.40	1.71

\* L-899 °C; M-1243 °C; H-1559 °C



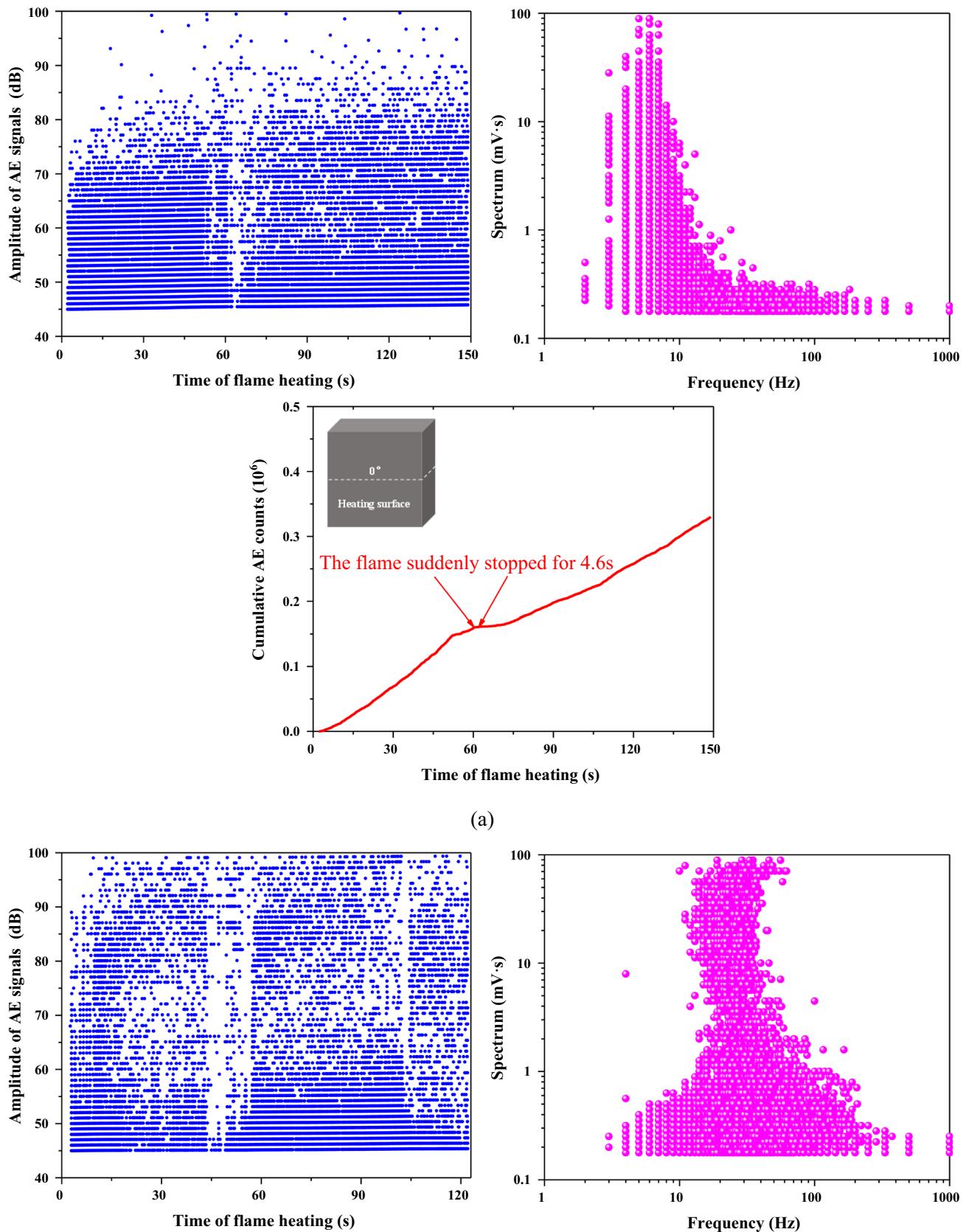


**Fig. 10** The AE signals recorded in the spallation process in the samples with bedding orientation of  $0^\circ$  (Fig. 5): **a** low temperature-899 °C; **b** medium temperature-1243 °C; **c** high temperature-1559 °C

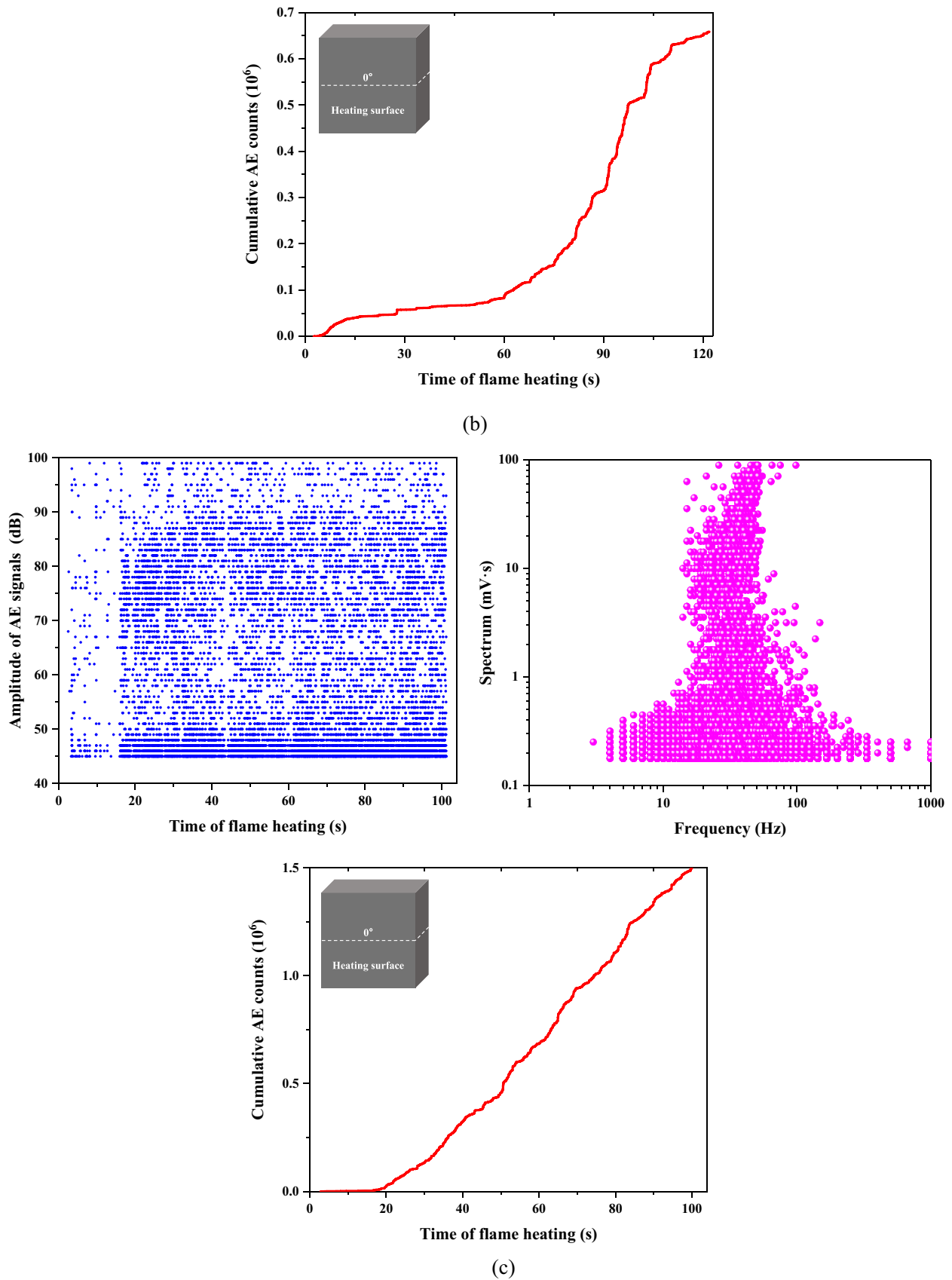


Fig. 10 continued

200 mm, 200 mm and 100 mm, respectively, Fig. 3c. In order to prevent the change in dry condition of sample and activation of bedding planes inside shale during cutting, no cooling solution was used for the cutting blades and rubber pads were installed between the shale block and the stationary support.

The shale contains developed bedding planes and complex mineral composition, and the dry density is roughly  $2700 \text{ kg/m}^3$ . The optical microscope picture and the rock composition obtained by the X-ray diffraction technique are shown in Fig. 4. The 9 prepared samples were divided into 3 group with 3 bedding directions, Fig. 5. Thermal and mechanical properties of the shale samples with these 3 bedding orientations have been measured in our previous work [7, 9, 10], Table 1.

## 2.2 Experimental setup and procedures

The experimental setup consists of a flame jet system, a surface temperature record system, an acoustic emission monitoring system and a videorecording system, Fig. 6. The flame jet system contains gas and oxygen tanks, delivery pipes, gas flow valve, pressure gauge, a combustion chamber and a flame nozzle, which can provide a maximum of approximately  $1800 \text{ }^\circ\text{C}$  of stable flame with diameter of 10 mm. The surface temperature recording system contains 4 thermocouples and an air temperature sensor, a controller and an upper linked computer. The 4 thermocouples and the air temperature sensor have the temperature measurement range of  $0\text{--}1300 \text{ }^\circ\text{C}$  and  $-200\text{--}1600 \text{ }^\circ\text{C}$ , respectively, with the accuracies of  $\pm 1\%$  and  $\pm 0.5\%$ , respectively; the acquisition time interval can be adjusted from 0.5 s to 1 h. For the present measurements, we selected the acquisition frequency of thermocouples as one per second. The air temperature sensor was only used to measure the flame temperature in the preliminary experiments. The PCI-2 acoustic emission (AE) system was used to monitor the thermal spallation. Only 1 sensor was used; the sampling frequency, threshold amplitude and amplification of preamplifier were set to 1 kHz–3 MHz, 45 dB and 40 dB, respectively. The videorecording system consists of two digital cameras with frame rate of 60 and 30 per second; the two cameras located near and far can be both controlled by a wireless Bluetooth controller. The overall experimental procedure is:

- (a) Connect all oxygen and gas pipes, prepare igniters, fix four thermocouple sensors on the upper, left, right and back surface of the sample, fix the camera at two proper positions and fix the AE sensor on the back surface of the sample.
- (b) Measure the wind speed at the outdoor test site. Experiments can begin only when the wind speed at the ground is less than  $0.5 \text{ m/s}$ .
- (c) Select a fixed trestle to put the flame nozzle and guarantee that the distance between the flame nozzle and flame heating surfaces are kept the same during flame heating for 9 samples. This aims at avoiding the effects of different distances between the flame and heating surfaces of samples.
- (d) Start the pressure gauge, flow valve and igniter, and the gas and oxygen into the nozzle at a gradually steady rate of combustion. For the whole experiment, different flame temperatures were to be achieved by controlling the gas and oxygen into the combustion chamber; the temperatures used are classified into high flame temperature ( $1559 \text{ }^\circ\text{C}$ ), medium flame temperature ( $1243 \text{ }^\circ\text{C}$ ) and low flame temperature ( $899 \text{ }^\circ\text{C}$ ). The exact values of these three flame temperatures were measured at the flame centre using an air temperature sensor with the measurement range of  $-200\text{--}1600 \text{ }^\circ\text{C}$  as described above.
- (e) When the determined flame temperatures are stabilized, place the burner with the fixed position of the nozzle. Simultaneously, notify the control host computer of the acoustic emission, camera and thermocouple to start recording the thermal spallation process.
- (f) End the experiment when either thermal fracturing is visible or thermal spallation stops.
- (g) Collect spalls above powder grade and derive AE, temperature records, and photographic data.

## 2.3 Observation and parameters of thermal spallation

### 2.3.1 Spallation

During the flame heating, the thermal spallation was recorded by two cameras. Figure 6 shows two representative thermal spallation moments when the continuous spallation occurred and spalls buckled out from the surface in high velocity with loud popping sounds. Increasing flame temperature enhanced the popping sounds and increased the ejection velocity. After a period of thermal spallation, the heating finished when the spallation stopped, or fractures normal to the heated surface emerged. Figures 7, 8, 9 show photographs of the final spallation stage of 9 shale samples with bedding orientations of  $0^\circ$ ,  $45^\circ$  and  $90^\circ$  under 3 flame temperatures. It can be seen that a roughly circular depression was produced by thermal spallation in each sample. All samples (except for a sample with the bedding orientation of  $90^\circ$  at low temperature)



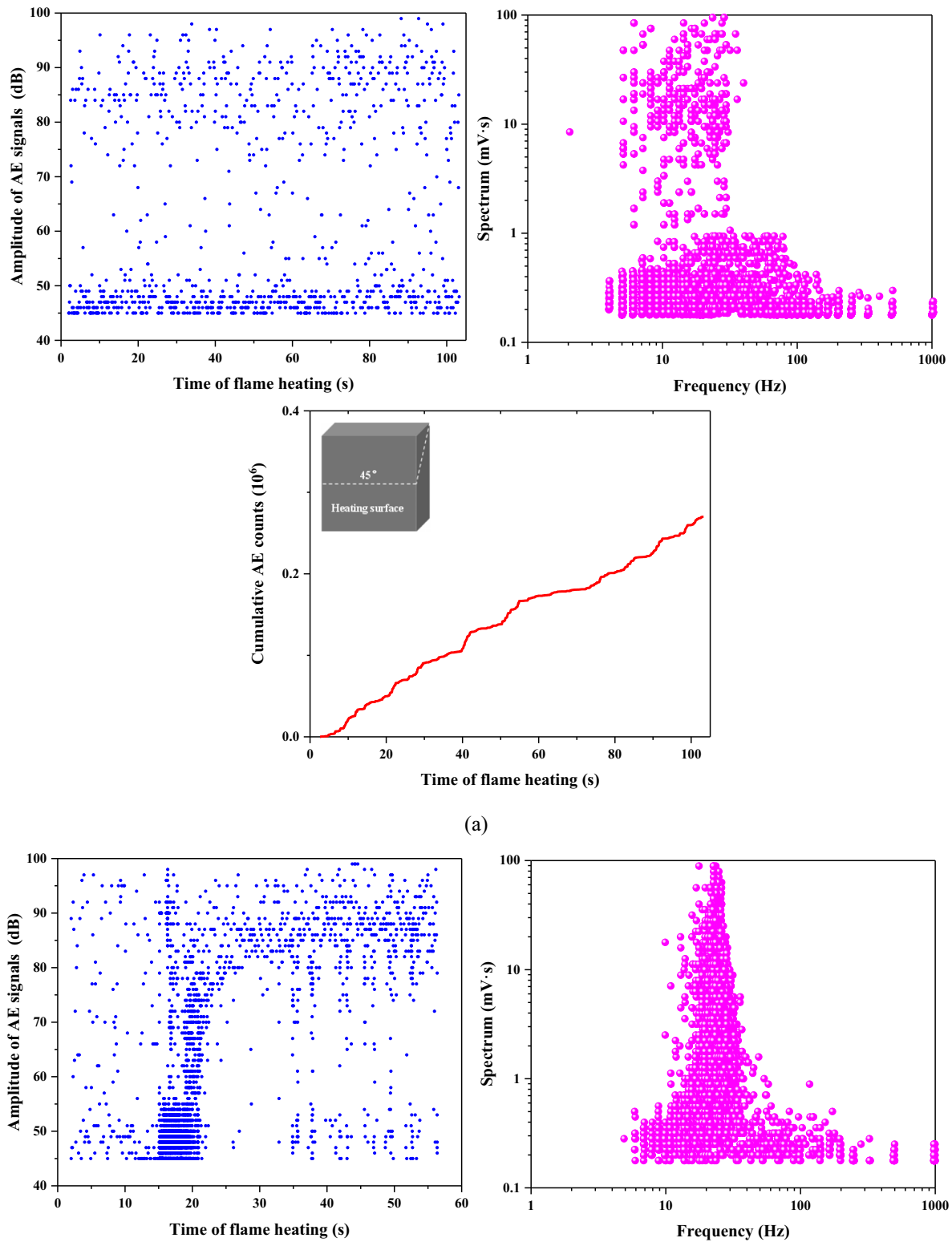


**Fig. 11** The AE signals recorded in the spallation process in the samples with bedding orientation of 45° (Fig. 5): **a** low temperature-899 °C; **b** medium temperature-1243 °C; **c** high temperature-1559 °C

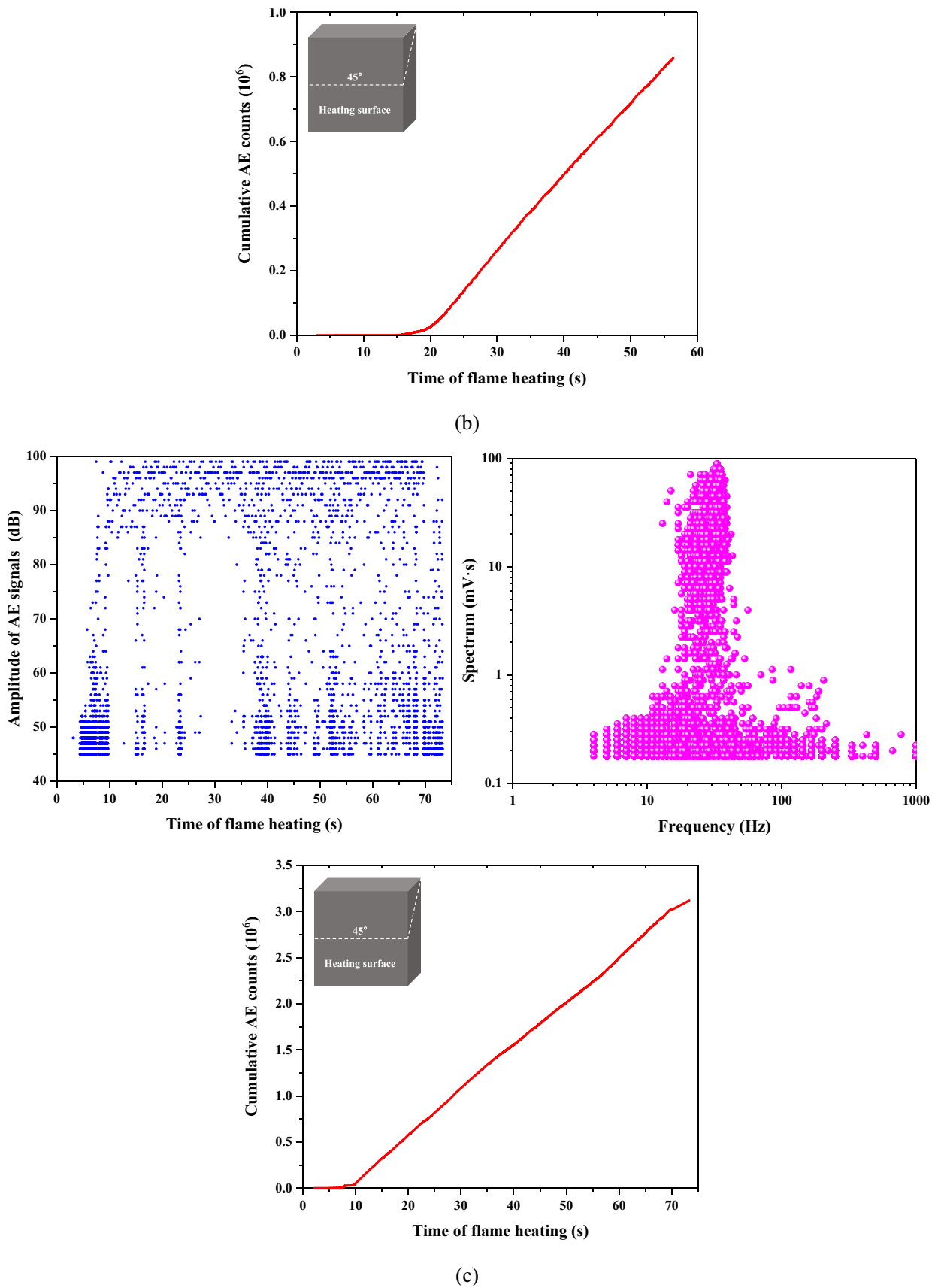
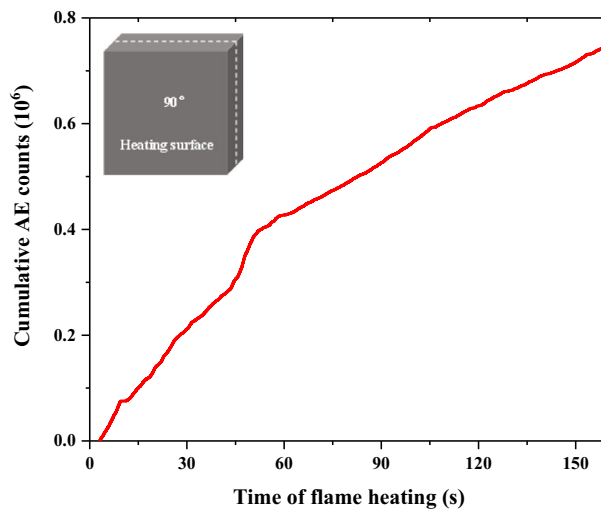
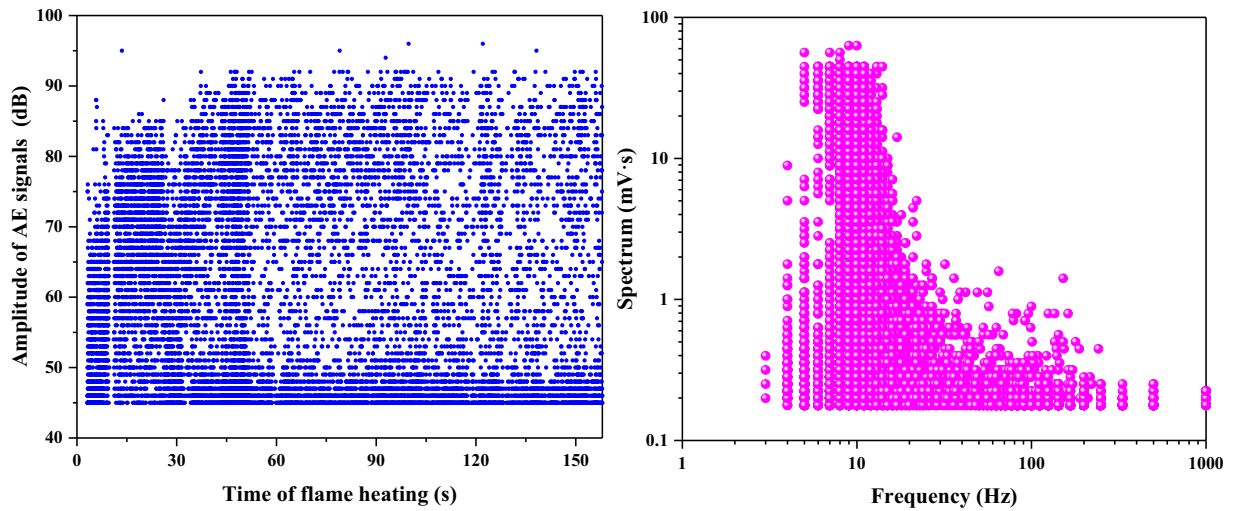
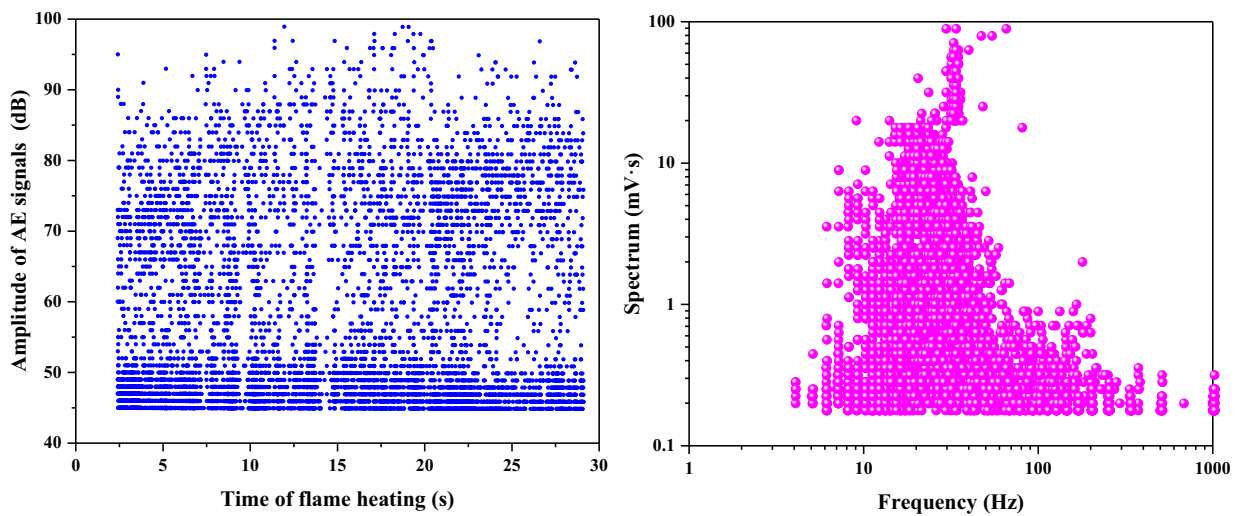


Fig. 11 continued



(a)



**Fig. 12** The AE signals recorded in the spallation process in the samples with bedding orientation of 90° (Fig. 5): **a** low temperature-899 °C; **b** medium temperature-1243 °C; **c** high temperature-1559 °C



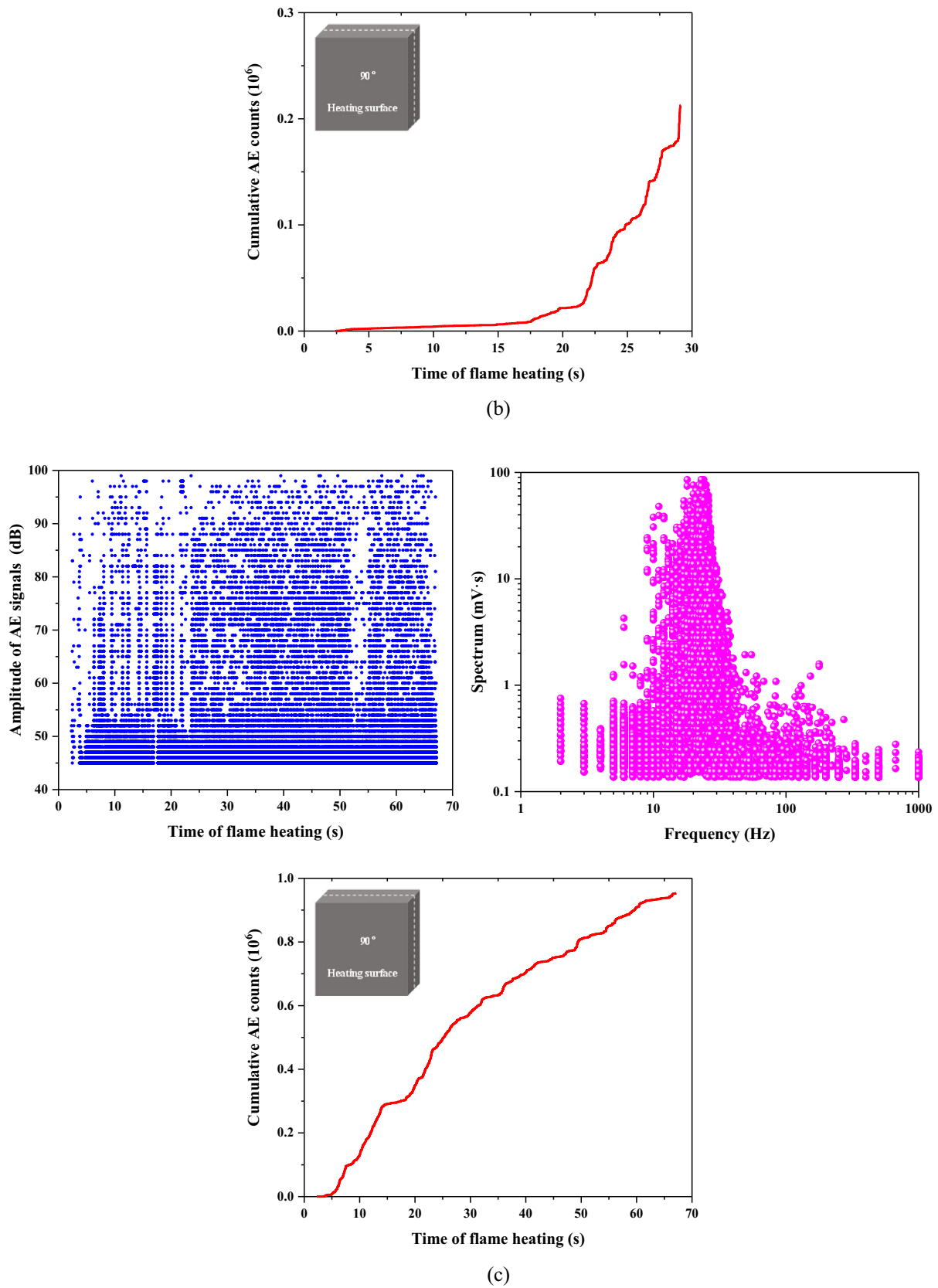


Fig. 12 continued

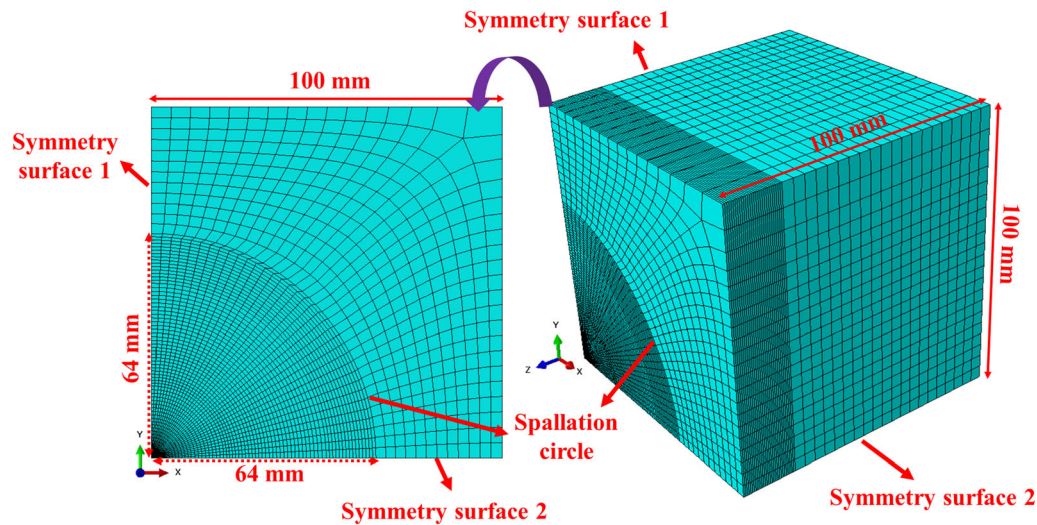


Fig. 13 The geometry and mesh condition for the quarter sample model

show the emergence of macroscopic fractures. These thermal fractures grew perpendicularly to the heated surface from the sample interior; their traces were affected by both flame temperature and bedding directions.

Table 2 lists the recorded spallation parameters and the dimensions of the spallation-produced depressions. The spallation (penetration) rate in Table 2 is the spallation depth increase per second. Generally, increasing flame temperature can reduce the spallation starting time, duration, depression diameter and depression depth, but increase the spallation rate. Notably, the spallation rate for the sample with bedding orientation of  $90^\circ$  at low flame temperature is the smallest, which may be a reason why no tensile fracture is created. As for the recorded moments of fracture emergence, it was not possible to capture the precise time of the first fracture appearance in the sample as there may be a view error and a delay in the moment when the fracture is noticed. Another observation in Fig. 6 is that only spalls produced by thermal spallation are observed; there were no traces of mineral melting in samples.

Previous literature tried to describe the effect of the flame temperature on the spall shape, weight, microstructure changes, mineral composition evolution and equivalent aspect ratio. However, given the assumption that spallation is caused by the crack-produced delamination with subsequent buckling of the surface layers (see Introduction) the most important parameters are the thickness and effective diameter of the spalls. Tables 3, 4 show the results of the measurements of these parameters for the 6 largest spalls above the powder grade for each of the 9 tested samples. As can be seen, increasing flame temperature gradually decreases the spalls thickness and

diameters. The bedding orientation only has a minor impact on these parameters, showing the least thickness of spallation in samples with bedding orientation of  $45^\circ$  independent of the flame temperature.

### 2.3.2 Acoustic emission

Figures 10, 11, 12 show the recorded amplitudes of AE signals, spectrum-frequency relationship and cumulative AE counts in the shale samples during thermal spallation, where the spectrum is based on the root-power (field) of Fourier Transform. From low to high flame temperature, the amplitude of the AE signals increases gradually, which is consistent with increasing severeness of the spallation process, i.e. louder popping sounds and more severe spalls ejections. The spectra show two characteristics: (1) the main frequency bands are within 200 Hz, which is the same as the simulated in-situ spallation in the laboratory [13]; (2) increasing the flame temperature leads to a certain increase in the pick frequency, showing the spectra gradually moving to the right in the horizontal axis. The cumulative AE counts are increasing monotonically as flame heating time increases, which suggests that the whole thermal spallation process is continuous. From the qualitatively different curves of cumulative AE counts, one can conclude that at a given flame temperature, the continuous thermal spallation may show different spallation intensities, which results in the spalls of different diameters and thicknesses and exact fractures. However, no significant correlation of AE signals with the bedding orientation can be detected.

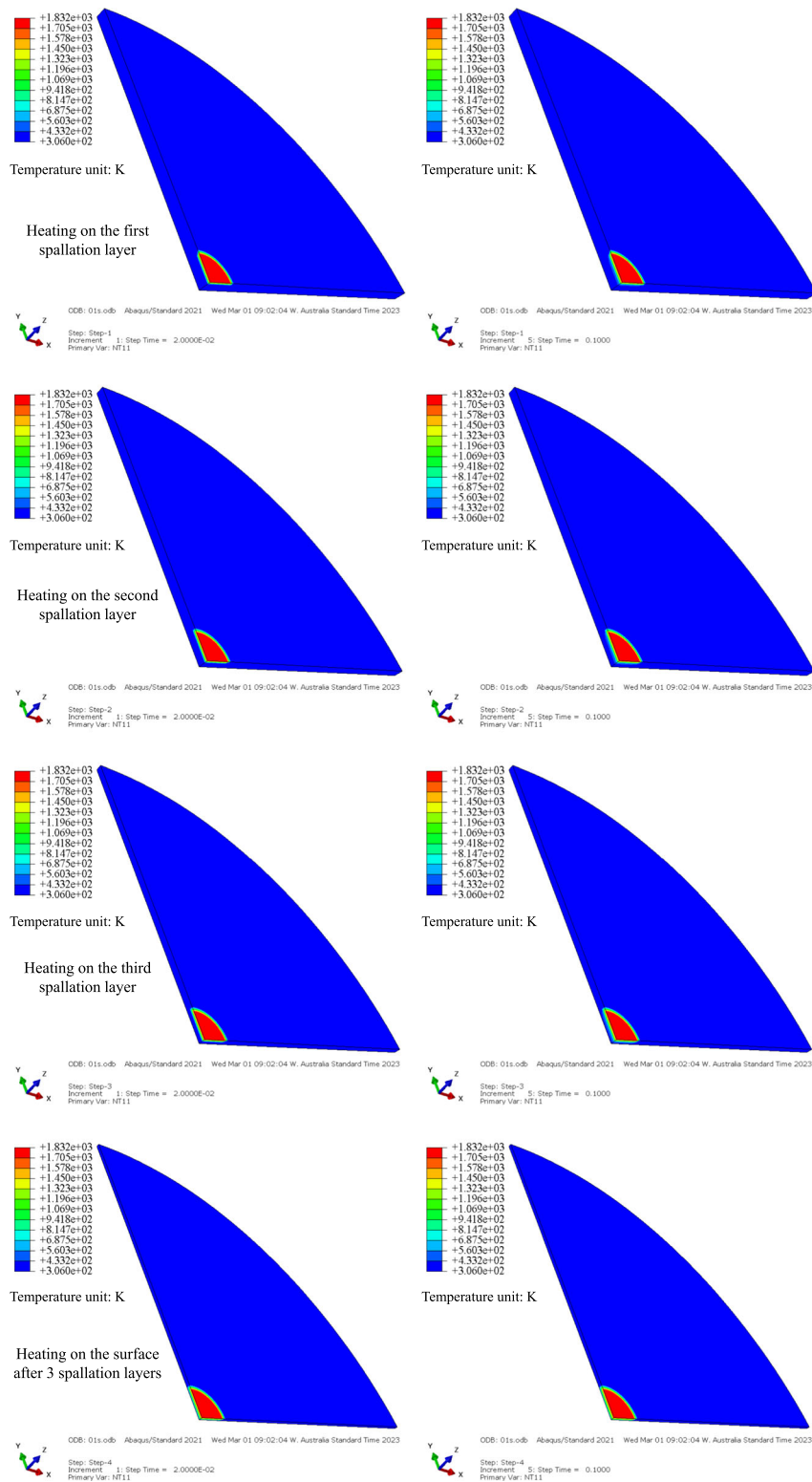


**Fig. 14** Temperature field of the model with 3 spallation steps under flame temperature of 1559 °C and time step (the time needed to remove a spallation layer) of 0.1 s



### 3 Finite element modelling

#### 3.1 Model description

To understand the temperature and stress fields induced in the shale samples during the thermal spallation process, 3D finite element modelling was carried out using ABAQUS 2021. For calculating thermal stresses, we assume that the material can be modelled as elastic. For thermal spallation the elastic formulation gives a healthy balance between simplicity and accuracy. The assumption about elasticity is

confirmed in Sect. 4 when the determined maximum stress magnitudes are compared with the UCS. Figures 7, 8, 9 show that the spallation areas are nearly circular. This suggests that there is an axial symmetry in the problem for all bedding plane orientations. Given that, it will be assumed, in the first approximation, that the material is isotropic both thermally and mechanically. For more complex, anisotropic constitutive equations used for localization and shear band see e.g. references [37, 50]. The flame action is modelled by a circular zone of the flame diameter to which the experimentally measured

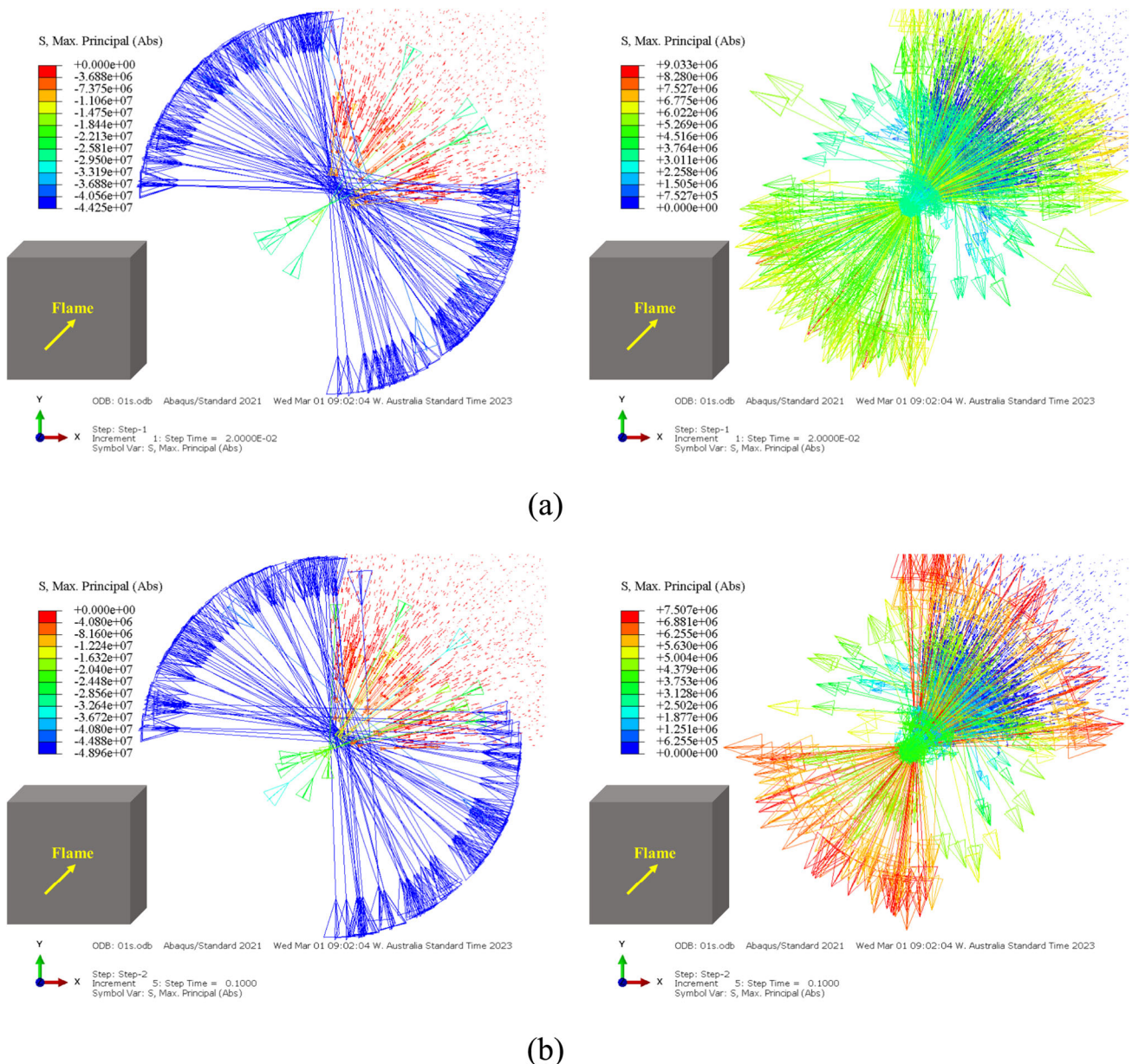


**Fig. 15** Induced maximum principal thermal stresses (in absolute value, Pa) in the model with 3 spallation steps under flame temperature of 1559 °C and time step (the time needed to remove a spallation layer) of 0.1 s: **a** step time (time from the beginning of heating) of 0.02 s and **b** step time of 0.2 s

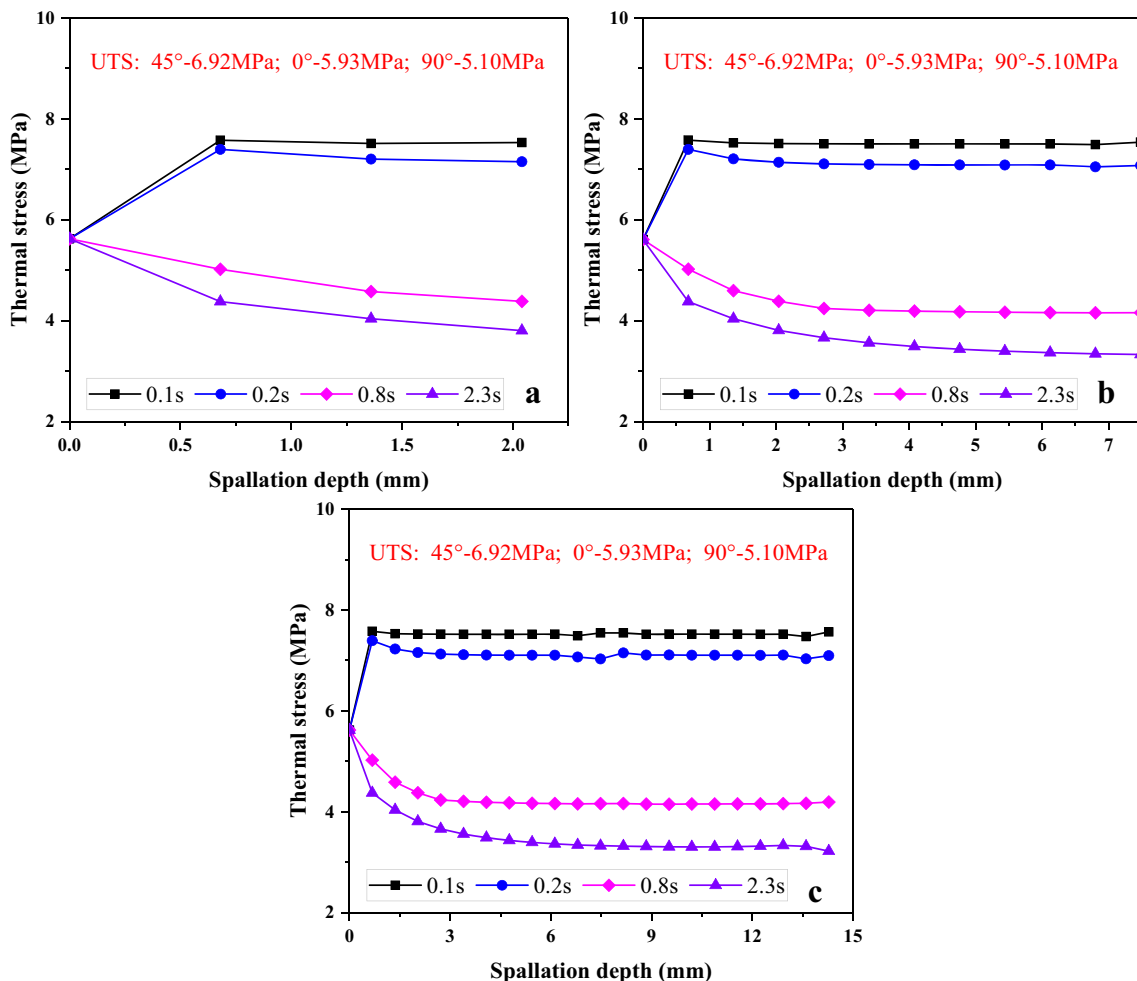


**Fig. 16** Simulated tensile thermal stresses in shale samples versus different spallation depth under flame temperature of 899 °C and 4 time steps after: **a** 3 spallation steps; **b** 11 spallation steps; **c** 21 spallation steps

flame temperature is applied. Considering the axial symmetry, only a quarter of the sample is modelled, Fig. 13. The model involves 144,793 elements (C3D8T) that are 8-node thermally coupled hexahedron, trilinear displacement and temperature.

The initial and boundary conditions are: the initial temperature is 33 °C (it is the weather temperature at the experiment site) for the whole model except the heated circle where the temperature is assumed to be equal to the measured flame temperature. Zero heat fluxes are set for Symmetry surfaces 1 and 2. There are heat transfer (transfer coefficient is 25 W/(m<sup>2</sup>•°C) and radiation (1.0 was set as radiation rate) between other surfaces and environment except the Symmetry surface 1, Symmetry surface 2, the flame area and the back surface (the temperature record of back surface remains at the same weather temperature). Mechanical boundary conditions are as follows. On Symmetry surface 1:  $U_x = 0$  and  $\tau_{xy} = \tau_{xz} = 0$ ; on Symmetry surface 2:  $U_y = 0$  and

$\tau_{xy} = \tau_{yz} = 0$ ; other surfaces have the normal and shear stresses equal to 0.

The photographs of the flame heating site and cumulative AE counts, Sect. 2, suggest that the thermal spallation process is continuous, characterized by ejection of spalls with different thicknesses. In this case, after the thin spalls are ejected from the samples, the flame will heat the newly created surface, which reinduces thermal stresses almost immediately. This continuous spallation process is modelled by sequential removal of several thin circular layers of diameter of the spallation depression. The layer thickness is 0.68 mm, which is the average spallation thickness observed in the experiments at low flame temperature, 899 °C. After the layer removal, the boundary conditions on the new surface are: the temperature of new surface is equal to the flame temperature and the new surface is free from load.

More difficult is to determine the spallation rate, since only the time of the first spallation can be exactly determined from the experimental records, Table 2. So, in the

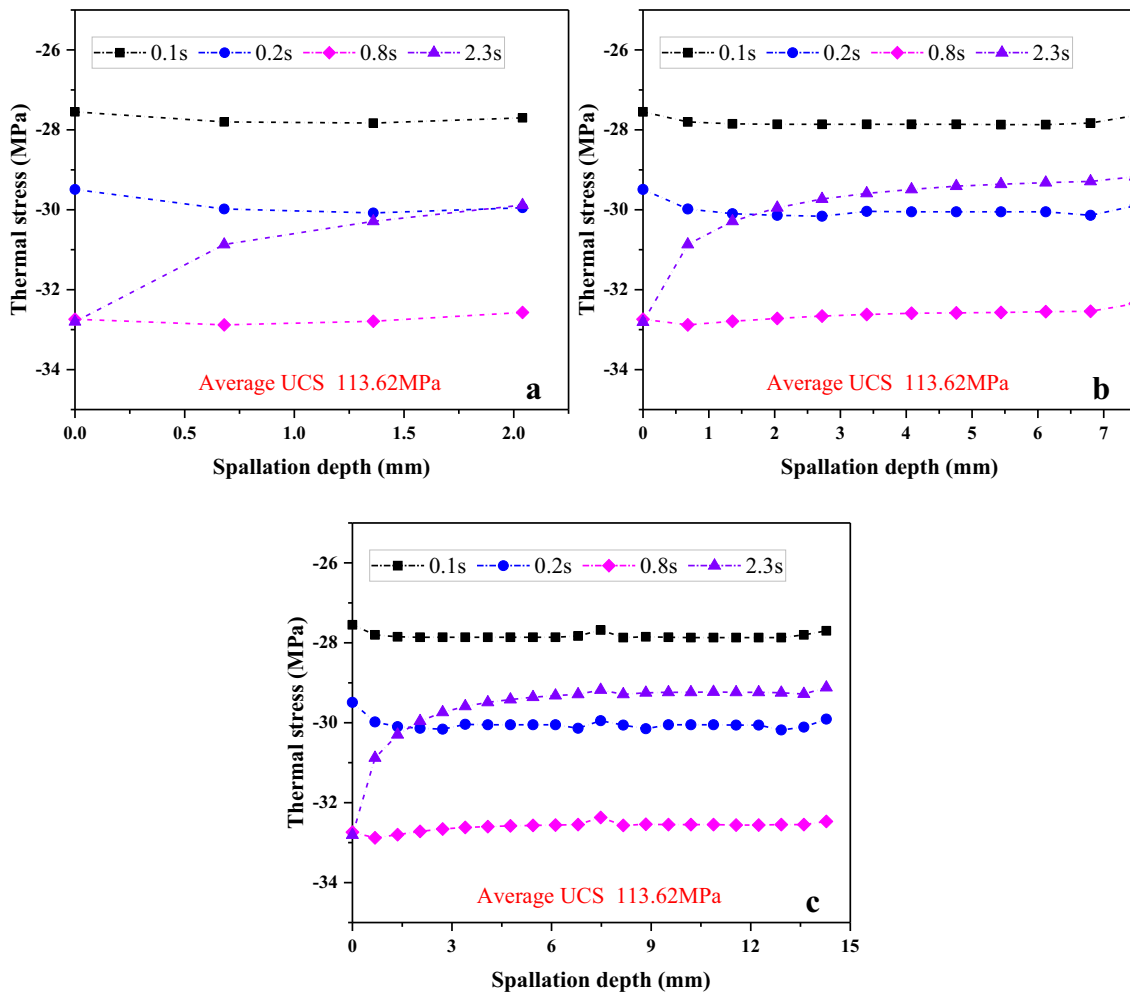


**Fig. 17** Simulated compressive thermal stresses in shale samples versus different spallation depth under flame temperature of 899 °C and 4 time steps after: **a** 3 spallation steps; **b** 11 spallation steps; **c** 21 spallation steps

modelling we tried different time steps (the time needed to remove a spallation layer) to see how this parameter impacts on the induced temperature and stress field characteristics.

### 3.2 Modelling results

Figure 14 shows the temperature fields for the model with 3 spallation steps (depths) under flame temperature of 1559 °C as functions of spallation time (and the depth). Obviously, except for the region around the flame zone, most part of the sample keeps constant temperature equal to the ambient temperature. It can be seen that the layer having high temperature is extremely thin and the continuous spallation process does not change this feature. With increasing spallation time (and the depth), the region affected by flame heating is still a surface thin layer with a roughly same depth and diameter, showing local heating nature of thermal spallation.

Figure 15 presents the maximum principal stresses (in absolute value) for the model with 3 spallation steps also under flame temperature of 1559 °C; the negative and positive numbers refer to compressive and tensile stresses, respectively. Generally, after putting the flame on the sample surface, the compressive stresses are generated at a thin surface layer, while the tensile stresses are induced under this thin compressed layer. With the continuous occurrence of spalls, the axisymmetric distribution of induced stresses stays the same, but the time step of spallation affects the stress values.

Figures 16, 17, 18, 19, 20, 21 show the simulated maximum thermal stresses (maximum principal stresses in absolute value) obtained during each spallation step for the model with 3, 11 and 21 spallation steps under 3 different flame temperatures and 4 time steps. Under each temperature, the ratios between the induced compressive and tensile stresses exhibit minor increase with increasing spallation depth. Changing the flame temperature does not

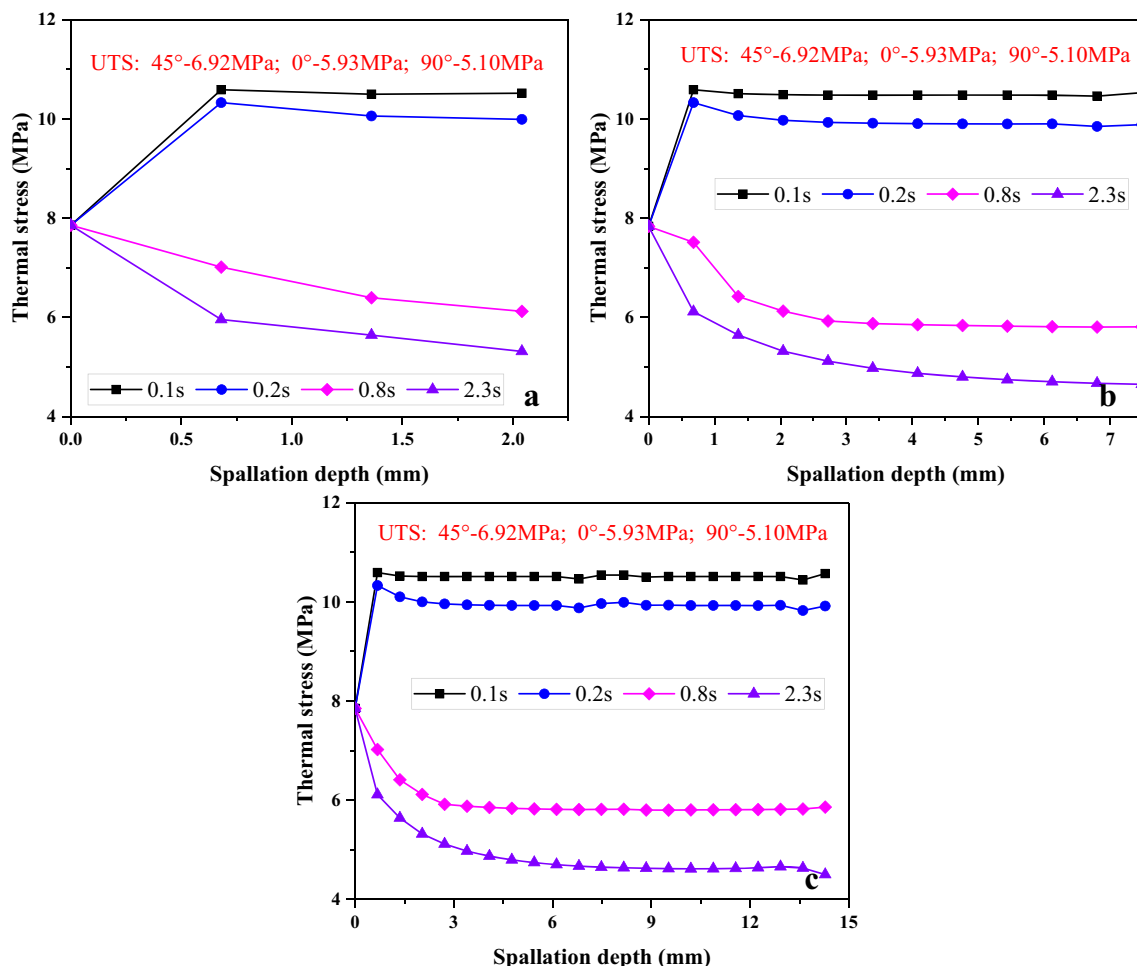


**Fig. 18** Simulated tensile thermal stresses in shale samples versus different spallation depth under flame temperature of 1243 °C and 4 time steps after: **a** 3 spallation steps; **b** 11 spallation steps; **c** 21 spallation steps

significantly change the ratios between the induced compressive and tensile stresses, but the ratios of compressive stress to the UCS are increased gradually, approximately from 29 to 51%. The evolution of induced stresses versus spallation depth shows a temperature-independent behaviour, which indicates that when the flame temperature is high enough to produce thermal spallation (but still under the melting point), the thermal spallation-induced stress evolution is not directly linked to the flame temperature.

As for the effect of the time step, the smaller the time step, the greater the tensile stress and the lower the compressive stress induced after the first spallation. Increasing the time step does not increase the compressive stress magnitude linearly; the largest compressive stress is seen at the time step of 0.8 s. Therefore, under a given thickness of spalls, a smaller spallation rate (larger time step) is less prone to induce a tensile fracture because smaller tensile stresses would be induced. This may be a reason for the absence of fracture for a sample with the bedding orientation of 90° under low flame temperature. Furthermore,

with increasing flame temperature, tensile fracture could be generated earlier after the flame application because the induced tensile stresses are larger than the average UTS value. This is a reason why the spallation duration and depth reduce with increasing flame temperature.

## 4 Discussion

We start with the analysis of the maximum magnitudes of computed tensile and compressive thermal stresses. The maximum tensile stress shown in Figs. 16, 18 and 20 reaches the magnitudes obviously exceeding the average uniaxial tensile strength (UTS), Table 1. Therefore, the tensile stresses generated under the spallation zone are generally sufficient to generate tensile fractures which are observed in all cases except one: the sample with bedding orientation of 90° under low flame temperature. It should be noted that the formation of tensile fractures could be affected by local fluctuations of tensile strength. This is a



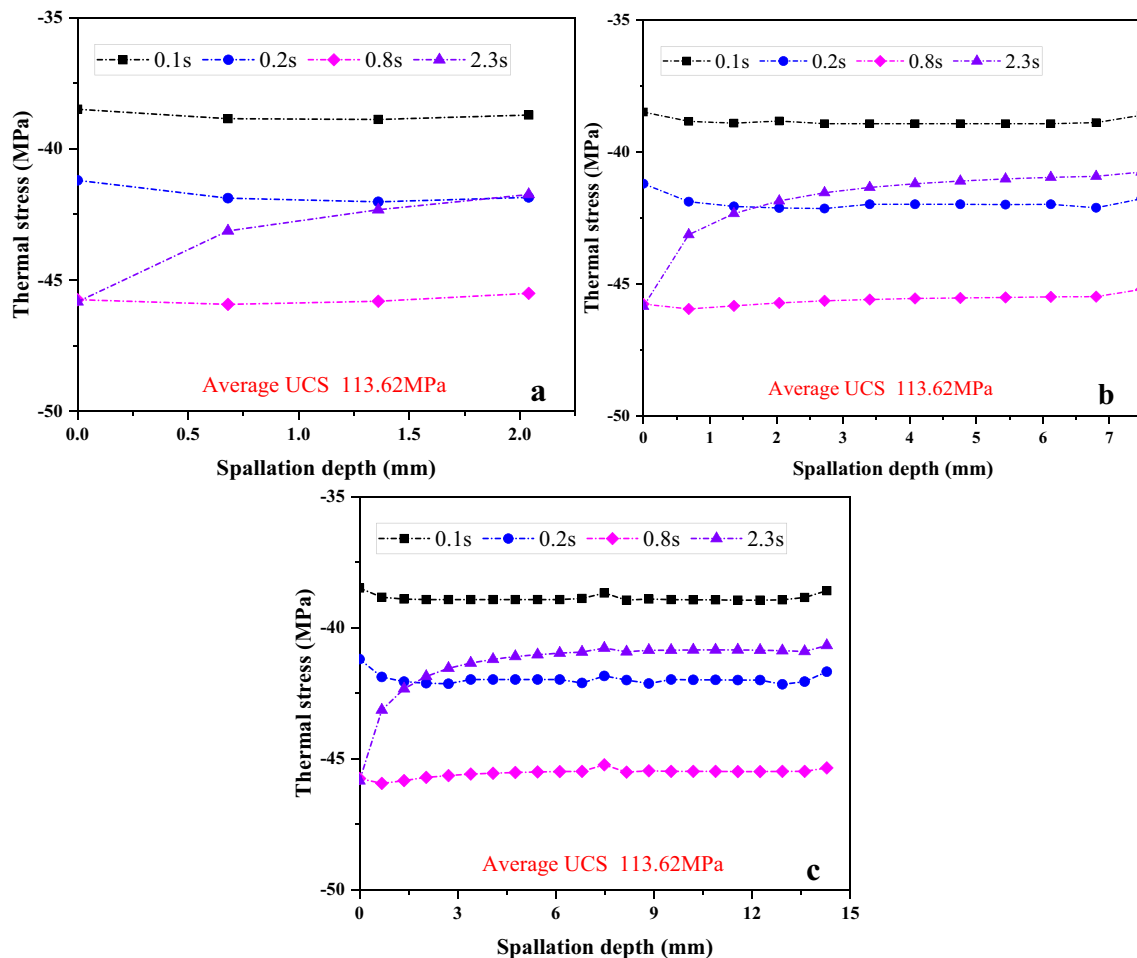


**Fig. 19** Simulated compressive thermal stresses in shale samples versus different spallation depth under flame temperature of 1243 °C and 4 time steps after: **a** 3 spallation steps; **b** 11 spallation steps; **c** 21 spallation steps

strong argument against the tensile fracture mechanism based on internal moisture: the internal water pressure is not needed for tensile fracture formation. After all, the shale samples tested were dried for 3 months still developing tensile fractures.

Consider now the maximum magnitudes of compressive thermal stresses. The modelling gives the following ranges, Table 5.

Given that the average UCS is 113.62 MPa the maximum compressive thermal stress magnitude is only 51% of UCS. Since considerable nonlinear effects in rocks under uniaxial compression start when the load is above half of UCS (as seen from the stress–strain curves of rock, e.g. Jaeger et al. [19]), one can conclude that the elastic model based on the assumption of elastic state of the shale samples can be accepted.

We now return to the assumed mechanism of thermal spallation: extensive fracture growth under compression acting parallel to the free surface, separating a thin layer from the bulk of the rock with subsequent layer buckling,

Fig. 2. This mechanism is similar to the spallation mechanism of a larger scale phenomenon – strain rockburst, e.g. references [4, 46]. It is remarkable that the stress of rockburst initiation is smaller than the rock UCS [1, 29, 31, 35]. Particularly, Martin et al. [28] found that the in situ spallation strength limit is only about  $40\% \pm 10\%$  of UCS. Recently, Wang et al. [46] have confirmed this spallation strength range by some analytical solutions from the theory of rock fracture mechanics. At the same time, our modelling also shows the spallation strength of thermal spallation to be about 29–51% of UCS matching the strength estimation for in situ spallation.

As discussed above, spallation is eventually caused by buckling of thin layers separated by fractures growing parallel to the free (and heated) surface under the action of major compressive principal stress. Given the axisymmetric compressive stress distribution and nearly axisymmetric shape of the spallation area this mechanism can be modelled by representing the separated layer as a circular plate buckled by the action of axisymmetric compressive stress.

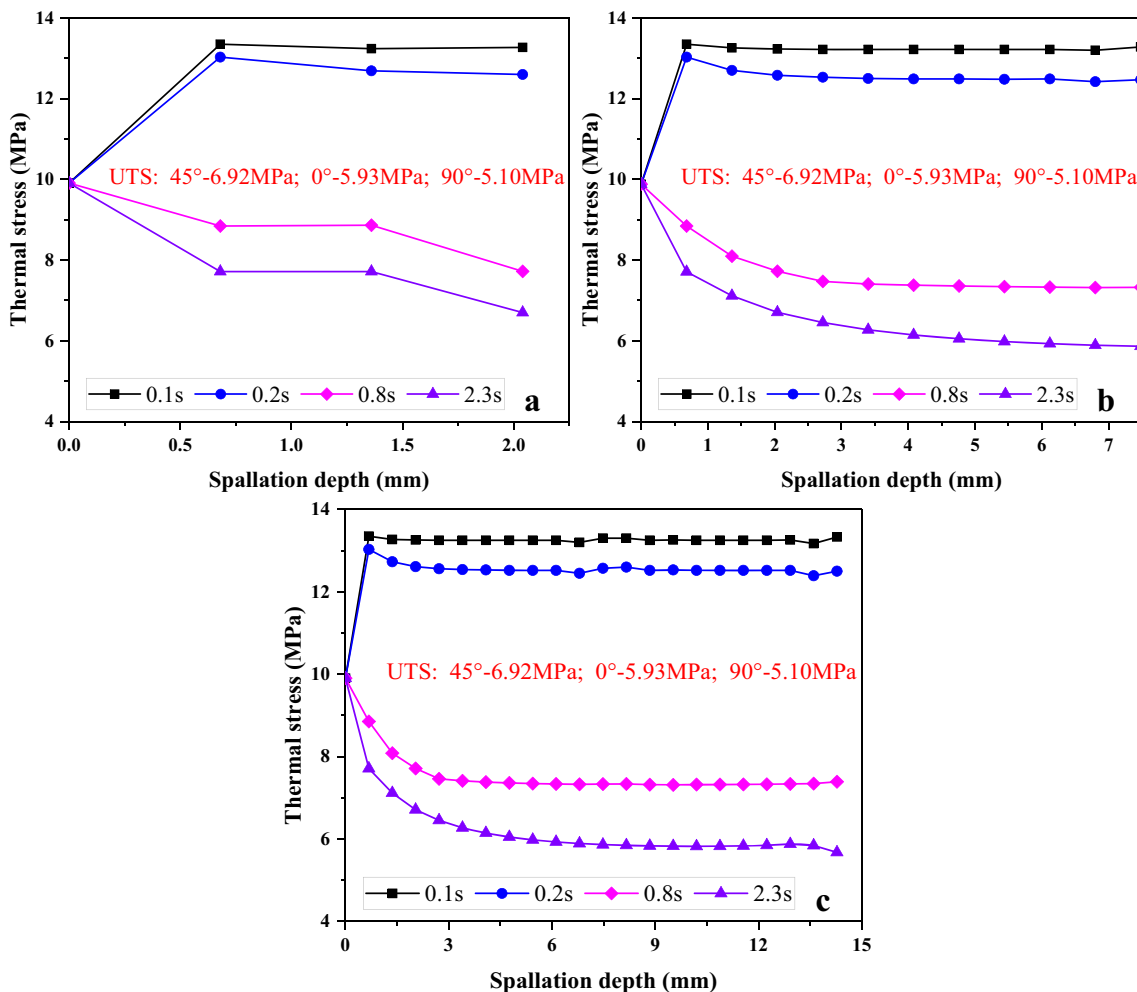


**Fig. 20** Simulated tensile thermal stresses in shale samples versus different spallation depth under flame temperature of 1559 °C and 4 time steps after: **a** 3 spallation steps; **b** 11 spallation steps; **c** 21 spallation steps

Calling the plate radius  $a$  and thickness (distance to the surface)  $h$  and assuming clumping of the plate edges the buckling stress reads (e.g. Timoshenko and Gere [41])

$$\sigma = 1.22 \frac{E}{1 - \nu^2} \left( \frac{h}{a} \right)^2 \tag{1}$$

where  $E$  and  $\nu$  are elastic modulus and Poisson’s ratio of shale samples,  $h$  is the thickness of spalls and  $a$  is the radius of the elastic buckling zone.

Given the measured thickness of the spallation,  $h = 0.68$  mm and the computed maximum magnitudes of compressive thermal stress, Figs. 17, 19 and 21, the buckling diameters  $d = 2a$  can be estimated. The results are presented in Fig. 22. These values are larger than the measured spall diameters shown in Table 4, which is natural, since the buckling leads to breakage of the buckling plate into smaller pieces. Nevertheless, the determined diameters are on par with the average measured diameters of the traces on the sample surface after thermal spallation,

which indicate the locally detached and buckled layers. Furthermore, the determined diameters are smaller than the diameters of spallation depression zones, which indicates that the thermal spallation should be of a mosaic nature. This can be seen as a surface nonuniformity after thermal spallation, Figs. 7, 8, 9. The surface nonuniformity of thermal spallation was also experimentally observed in [17, 36].

It should be noted that we only modelled the flame circle with the diameter of the burner without considering the flame spread on the heating surface of the sample. The spread, however, exists when a flame is jetted on a fixed wall [3]. Based on the flame temperature distribution [51], where the spread of flames only causes a larger flame circle on the wall covered by nearly the same temperature, we further set the measured flame temperature on the entire spallation depression for computation of thermal stresses. Figure 23 shows the computed contours of maximum principle thermal stresses (in absolute value) for the model

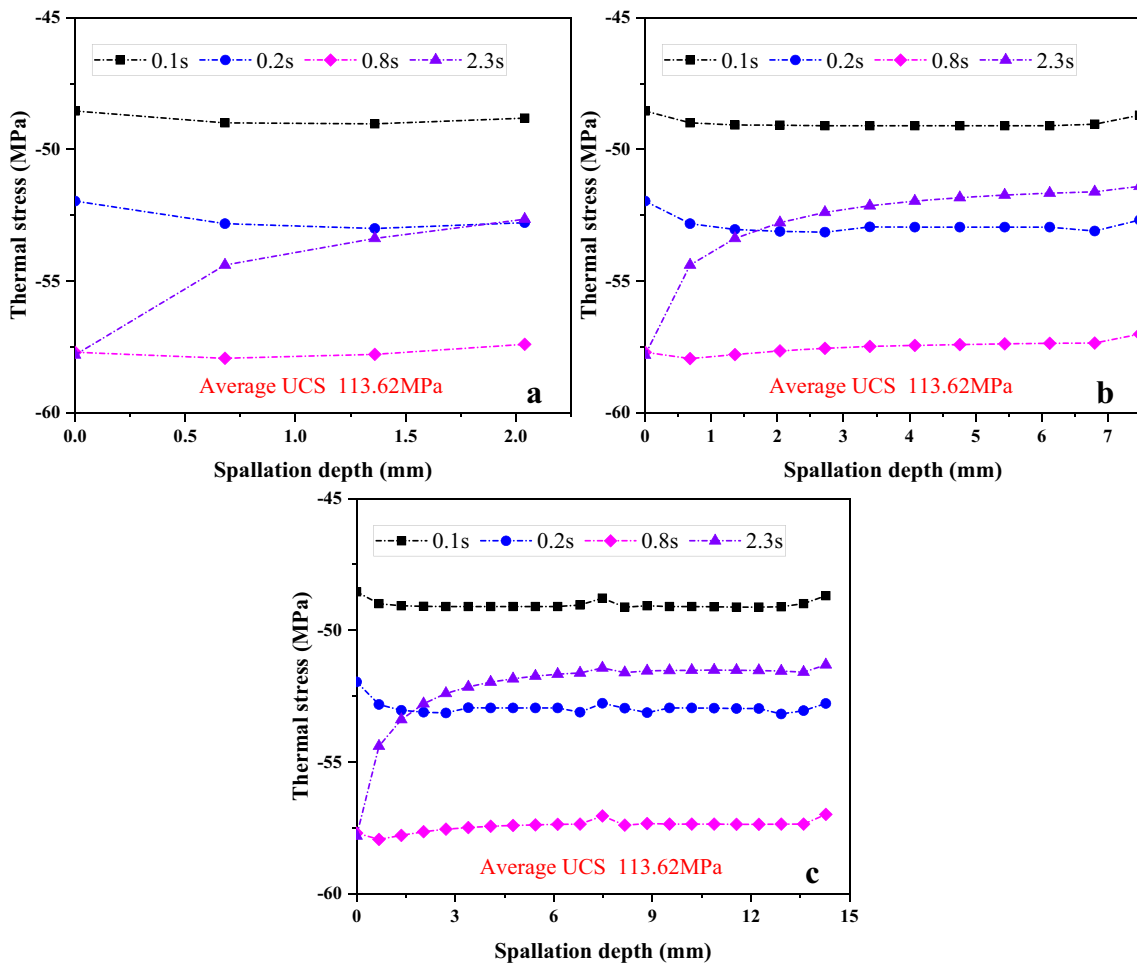


**Fig. 21** Simulated compressive thermal stresses in shale samples versus different spallation depth under flame temperature of 1559 °C and 4 time steps after: **a** 3 spallation steps; **b** 11 spallation steps; **c** 21 spallation steps

**Table 5** Computed maximum compressive thermal stress magnitudes

Flame temperature, °C	Compressive thermal stress magnitude, MPa
899	28–33
1243	38–46
1559	49–58

with the flame spread on the heating surface under flame temperature of 1559 °C and time step of 0.1 s. As can be seen, thermal stress magnitudes are almost the same as in the model without the flame spread, Figs. 20 and 21. The maximum compressive stress covers the spallation depression zone, indicating that the entire spallation zone can buckle under this stress. Spalls flying away could produce the turbulent flow which affects the gas flow such that the flame temperature distribution will only be changed locally [3]. This could result in producing separate buckling zones with the diameters shown in Fig. 22. This

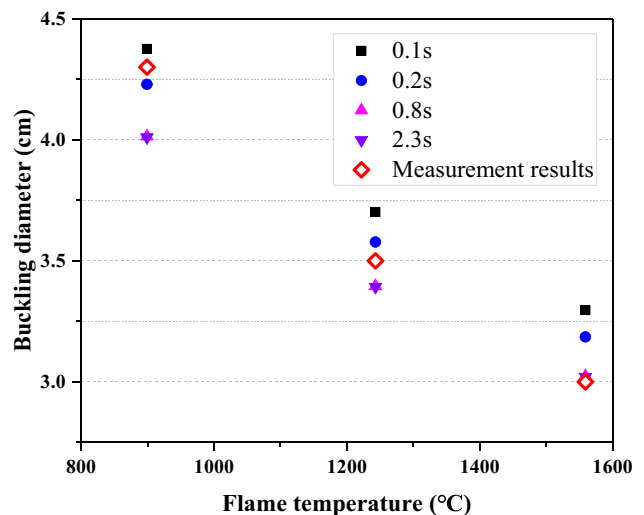


**Fig. 22** Computed buckling diameter of clamped elastic circular plate versus flame temperatures under 4 time steps. The spall thickness is assumed to be 0.68 mm and the corresponding average measured diameters of the spalling trace of local depression surface in the samples after thermal spallation

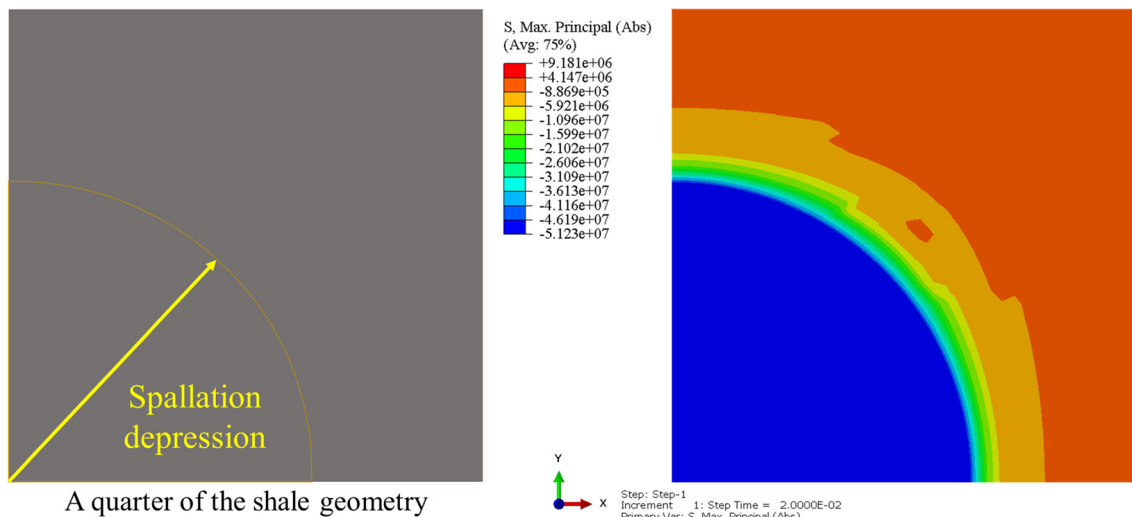


**Fig. 23** The simulated maximum principle thermal stresses (in absolute value, Pa) for the model account for flame spread on the heating surface under 1559 °C and time step of 0.1 s

**Table 6** Drilling information statistics for three production wells in Longmaxi shale reported in the references [2, 52]

Well name	Horizontal drilling sage (m)	Reservoir temperature ( °C)	Drilling bite	Drilling speed (m/h)	Drilling period (d)	Borehole diameter (mm)
Lu 202	3900–6905	> 140	PDC bit	1.57	178.53	215.9
Lu 203	3340–5600	> 145	PDC bit	2.05	106.99	215.9
CS1	–	Around 180	PDC bit	0.50	–	241.3

**Table 7** The evaluation of thermal spallation rate by comparing to real conventional drilling speeds

Flame temperature ( °C)	Speed (cm/s)	Evaluation (comparison to real well drilling)			Speed (cm/s)	Evaluation (comparison to real well drilling)		
		To Lu 202	To Lu 203	To CS1		To Lu 202	To Lu 203	To CS1
899	0.0281	0.64	0.49	2.02	0.0360	0.83	0.63	2.59
1243	0.0324	0.74	0.57	2.05	0.0411	0.94	0.72	2.60
1559	0.0382	0.88	0.67	2.41	0.0425	0.97	0.75	2.68

way, the mechanics of mosaic nature of thermal spallation of rocks can be explained.

Also, we should note that the thermal spallation rates of 9 dry shale samples in Table 2 are comparable with conventional mechanical drilling speeds in the same Longmaxi shale. The real conventional mechanical drilling information obtained from references [2, 52] is listed in Table 6; these three wells are the typical deep wells in the same Longmaxi shale, Changning-Weiyuan shale gas extraction site in Sichuan Basin where we excavated our samples. Table 7 shows the comparisons of our thermal spallation rate under three flame temperatures to these conventional mechanical drilling speeds. As can be seen all our thermal

spallation rates under three flame temperatures are near or even exceed the mechanical drilling speeds, which indicates the competitiveness of thermal spallation drilling. Moreover, with the increasing buried depth of the Longmaxi shale, the deep mechanical drilling at horizontal stage meets considerable challenges such as the low drilling speed, the difficulty with precise control of drilling trajectory, drilling pipe sticking, frequent trip and severe wear of drilling bits [14]. Even, the drilling sticking period was reported to be 50 days for the Z201 well, which increased the cost and limited the extraction efficiency [33].

Furthermore, the presence of high geo-stresses can suppress the formation of tensile fractures parallel to the



flame direction which are detrimental to the process of thermal spallation, Fig. 2. Subsequently, the thermal spallation drilling can be an ideal method that is technically feasible and economically beneficial for shale gas extraction. Parametric analysis of thermal stress distributions in transversal isotropic material was conducted in our recent paper focussing on anisotropy of thermal spallation of rocks [11], which can also help design the exact thermal spallation drilling method in deep anisotropic shale reservoirs. Notably, there are still two main factors that can possibly affect the thermal spallation drilling speed of deep shale, pore water [24] and thermal damages induced by in situ temperature [37]. Under the bottom of vertical well (horizontal stage), the in situ temperature of Longmaxi shale with depth over 3500 m (like Lu 202 well and Lu 203 well) is confirmed to be over 100 °C [18]. Guo et al. [10] showed the reservoir temperature of 100–200 °C covers the largest buried depth range of 3500–7000m for this Longmaxi shale. Future work is planned to investigate the effect of the in situ stress, temperature and pore water on the thermal spallation rate.

## 5 Conclusions

Experiments on thermal spallation of dry shale samples with bedding orientations of 0°, 45° and 90° under open flame show that continuous thermal spallation is induced with obvious ejection of different spalls and popping sounds. Increasing the flame temperature promotes the ejection, popping sounds and spallation rate. This is consistent with the characteristics of recorded AE pulses. Furthermore, increasing the flame temperature decreases the starting moment of thermal spallation, spallation duration, and the spallation depression diameter and depth. Tensile fractures are also observed in the shale samples growing perpendicular to the heated surface. The only case when the tensile fractures were not observed was a sample with bedding orientation of 90° under the low flame temperature.

Thermal elastic 3D finite element modelling shows that the induced tensile stresses are close to the average tensile strength of the shale samples. The continuous spallation process from the beginning of flame action to the spallation end little changes the axisymmetric distribution of induced stress field. Under each temperature, the ratios between the induced compressive stress and tensile stress increase marginally with the increasing spallation depth. Changing the flame temperature cannot significantly change the proportional relation between induced compressive and tensile stress, but the ratio of induced compressive stress to the UCS of samples increases, from 29 to 51%. The time step of the formation of each spallation depth has an

obvious impact on both tensile and compressive thermal stresses, showing that increasing the time step increases the induced tensile stress; the largest compressive stress occurs at the time step of 0.8 s.

The thermal spallation of rocks produced by surface heating is eventually caused by buckling of thin layers separated from the bulk of the rock by fractures extensively growing under the compressive thermal stress. Estimation of the dimensions of the buckled layer shows that they are smaller than the diameter of the spallation depression area, therefore the thermal spallation should be of a mosaic nature which is confirmed to be produced by the flame spread on the heating surface. Furthermore, the relationship between the spallation strength and the UCS of rocks in our thermal spallation is found to be within the accepted spallation strength range for in-situ spallation (e.g. strain rockburst). Thermal spallation rates of shale samples are comparable with the conventional drilling speeds in the real shale gas extraction projects.

The obtained results are important for further understanding the mechanics of thermal spallation. They can also assist in understanding large-scale spallation-like processes in the Earth's crust and designing rock drilling and cutting techniques based on thermal spallation, especially at high depths.

**Acknowledgements** YG thanks the China Scholarship Council for overseas study support (No. 202106370160). AVD and EP acknowledge support from the Australian Research Council through project DP210102224. We also want to thank Mr. Shili Li for his help on our experimental work and thank the UWA IT service for providing the calculating platform.

**Data availability** The datasets generated during and/or analysed during the current study are available from the corresponding author on reasonable request.

## Declarations

**Conflict of interest** The authors declare that they have no known competing financial interests or personal relationships that could have appeared to influence the work reported in this paper.

## References

- Andersson JC, Martin CD, Stille H (2009) The Äspö pillar stability experiment: Part II—rock mass response to coupled excavation-induced and thermal-induced stresses. *Int J Rock Mech Min Sci* 46(5):879–895
- Deng H, Jia L (2022) Key technologies for drilling deep and ultra-deep wells in the Sichuan Basin: current status, challenges and prospects. *Nat Gas Ind* 42(12):82–94
- Dong LL, Leung CW, Cheung CS (2004) Heat transfer and wall pressure characteristics of a twin premixed butane/air flame jets. *Int J Heat Mass Transf* 47(3):489–500

4. Dyskin A, Pastenak E, Wang H, Dight P (2020) Skin rockbursts and microseismicity in underground mining. In: EAGE 2020 Annual Conference & Exhibition Online, vol. 2020, p. 1–5
5. Freeman D, Sawdye J, Mumpton F (1963) The mechanism of thermal spalling in rocks. *Colo Sch Mines Q* 58(4):225–252
6. Germanovich L (1997) Thermal spalling of rock. *Adv Fract Res* 6:2771–2782
7. Guo Y, Huang L, Li X, Chen J, Sun J (2020) Experimental investigation on the effects of thermal treatment on the physical and mechanical properties of shale. *J Nat Gas Sci Eng* 82:103496
8. Guo Y, Li X, Huang L, Liu H, Wu Y (2021) Effect of water-based working fluid imbibition on static and dynamic compressive properties of anisotropic shale. *J Nat Gas Sci Eng* 95:104194
9. Guo Y, Li X, Huang L (2022) Changes in thermophysical and thermomechanical properties of thermally treated anisotropic shale after water cooling. *Fuel* 327:125241
10. Guo Y, Huang L, Li X (2023) Experimental investigation of the tensile behavior and acoustic emission characteristics of anisotropic shale under geothermal environment. *Energy* 263:125767
11. Guo Y, Dyskin A, Pasternak E (2024) Thermal spallation of dry rocks induced by flame parallel or normal to layering: effect of anisotropy. *Energy* 288:129697
12. Hasenjäger (1935) Zur Frage der Abplatzungen an Betonbauteilen aus Normalbeton bei Brandbeanspruchung. Braunschweig, Germany
13. He MC, Miao JL, Feng JL (2010) Rock burst process of limestone and its acoustic emission characteristics under true-triaxial unloading conditions. *Int J Rock Mech Min Sci* 47(2):286–298
14. He X, Chen G, Wu J, Liu Y, Wu S, Zhang J, Zhang X (2023) Deep shale gas exploration and development in the southern Sichuan Basin: new progress and challenges. *Nat Gas Ind B* 10(1):32–43
15. Hertz KD (2003) Limits of spalling of fire-exposed concrete. *Fire Saf J* 38(2):103–116
16. Hertz KD, Sørensen LS (2005) Test method for spalling of fire exposed concrete. *Fire Saf J* 40(5):466–476
17. Hu X, Song X, Liu Y, Li G, Shen Z, Lyu Z (2018) Aspect ratio of spalls of granite in flame-jet spallation and its effect on the modeling prediction of spallation properties. *J Petrol Sci Eng* 171:1390–1399
18. Huang L, Guo Y, Li X (2022) Mechanical response to dynamic compressive load applied to shale after thermal treatment. *J Nat Gas Sci Eng* 102:104565
19. Jaeger JC, Cook NGW, Zimmerman R (2009) Fundamentals of rock mechanics. Wiley-Blackwell, London, Oxford
20. Jansson R, Boström L (2009) The influence of pressure in the pore system on fire spalling of concrete. *Fire Technol* 46(1):217
21. Kant MA, von Rohr PR (2016) Minimal required boundary conditions for the thermal spallation process of granitic rocks. *Int J Rock Mech Min Sci* 84:177–186
22. Kant MA, Rossi E, Madonna C, Hoser D, von Rohr PR (2017) A theory on thermal spalling of rocks with a focus on thermal spallation drilling. *J Geophys Res-Solid Earth* 122(3):1805–1815
23. Kendrick KJ, Partin CA, Graham RC (2016) Granitic boulder erosion caused by chaparral wildfire: implications for cosmogenic radionuclide dating of bedrock surfaces. *J Geol* 124(4):529–539
24. Khor HC, Dyskin AV (2003) Mechanisms of thermal fracturing and spallation in cementitious materials. *Aust J Mech Eng* 1(1):1–4
25. Kömle NI, Weiss P, Yung KL (2008) Considerations on a suction drill for lunar surface drilling and sampling: i feasibility study. *Acta Geotech* 3(3):201–214
26. Lyu Z, Song X, Li G, Wang G, Shi Y, Liu Y, Zheng R (2018) Experimental analysis on characteristics of micro-structure and mineralogy changes in thermal spallation drilling. *J Petrol Sci Eng* 167:100–109
27. Maier M, Saxer A, Bergmeister K, Lackner R (2020) An experimental fire-spalling assessment procedure for concrete mixtures. *Constr Build Mater* 232:117172
28. Martin CD, Kaiser PK, McCreath DR (1999) Hoek–Brown parameters for predicting the depth of brittle failure around tunnels. *Can Geotech J* 36(1):136–151
29. Martin CD, Christiansson R (2009) Estimating the potential for spalling around a deep nuclear waste repository in crystalline rock. *Int J Rock Mech Min Sci* 46(2):219–228
30. Miura T, Nakamura H, Yamamoto Y (2023) Expansive spalling mechanism of concrete due to high temperature based on developed hygro-thermal-mechanical model by 3D-RBSM-TNM. *Eng Fract Mech* 284:109216
31. Pelli F, Kaiser PK, Morgenstern NR (1991) An interpretation of ground movements recorded during construction of the Donkin–Morien tunnel. *Can Geotech J* 28(2):239–254
32. Preston F, White H (1934) Observations on spalling. *J Am Ceram Soc* 17(1–12):137–144
33. Qi Y, Fan S, Yu L Innovation and practice of efficient drilling technology for deep shale gas. In: 11th Asia-Pacific Shale & Unconventional Resources Summit. Shanghai vol. 2021, p. 49–54
34. Rauenzahn R, Tester J (1985) Flame-jet induced thermal spallation as a method of rapid drilling and cavity formation. In: SPE Annual Technical Conference and Exhibition, Las Vegas, Nevada SPE-14331-MS
35. Read RS, Chandler NA, Dzik EJ (1998) In situ strength criteria for tunnel design in highly-stressed rock masses. *Int J Rock Mech Min Sci* 35(3):261–278
36. Rossi E, Jamali S, Saar MO, Rudolf von Rohr P (2020) Field test of a combined thermo-mechanical drilling technology. Mode I: thermal spallation drilling. *J Pet Sci Eng* 190:107005
37. Semnani SJ, White JA, Borja RI (2016) Thermoplasticity and strain localization in transversely isotropic materials based on anisotropic critical state plasticity. *Int J Numer Anal Meth Geomech* 40(18):2423–2449
38. Smith A, Pells P (2008) Impact of fire on tunnels in Hawkesbury sandstone. *Tunn Undergr Space Technol* 23(1):65–74
39. Sun Q, Liu Y, Shen Z, Han Y, Wang Q, Liu P (2022) A combined thermal spallation and melting technology by plasma jet for deep and hard rock reservoirs. *SPE J* 28(1):49–63
40. Thirumalai K (1969) Process of thermal spalling behavior in rocks an exploratory study. In: The 11th U.S. Symposium on Rock Mechanics (USRMS), Berkeley, California: ARMA-69–0705
41. Timoshenko SP, Gere JM (1961) Theory of elastic stability, 2nd edn. McGraw-Hill Book Company, New York
42. Vogler D, Walsh SDC, von Rohr PR, Saar MO (2020) Simulation of rock failure modes in thermal spallation drilling. *Acta Geotech* 15(8):2327–2340
43. Walsh SDC, Lomov IN (2013) Micromechanical modeling of thermal spallation in granitic rock. *Int J Heat Mass Transf* 65:366–373
44. Walsh SDC, Lomov IN, Wideman TW, Potter JM (2014) Size dependent spall aspect ratio and its effects in thermal spallation. *Int J Rock Mech Min Sci* 70:375–380
45. Wang G, Radziszewski P, Ouellet J (2008) Particle modeling simulation of thermal effects on ore breakage. *Comput Mater Sci* 43(4):892–901
46. Wang H, Dyskin A, Pasternak E, Dight P, Jeffcoat-Sacco B (2022) Fracture mechanics of spallation. *Eng Fract Mech* 260:108186
47. Wilkinson MA, Tester JW (1993) Experimental measurement of surface temperatures during flame-jet induced thermal spallation. *Rock Mech Rock Eng* 26(1):29–62
48. Williams R, Dey T, Rauenzahn R, Kranz R, Tester J, Potter R, Murphy H (1988) Advancements in thermal spallation drilling

- technology. Los Alamos National Lab, NM (USA). LA-11391-MS
49. Zeiml M, Lackner R, Mang HA (2009) Experimental insight into spalling behavior of concrete tunnel linings under fire loading. *Acta Geotech* 3(4):295–308
  50. Zhao Y, Borja RI (2022) A double-yield-surface plasticity theory for transversely isotropic rocks. *Acta Geotech* 17(11):5201–5221
  51. Zhen HS, Chen KD, Chen ZB, Wei ZL, Fu LR (2023) Heat transfer analysis of impinging flames using field synergy principle. *Case Stud Therm Eng* 43:102807
  52. Zheng S, Xie X, Luo L, Jing Y, Tang M, Yang R, Zhong G, Wang J, Chen Z (2019) Fast and efficient drilling technologies for deep shale gas horizontal wells in the Sichuan Basin: a case study of Well Lu 203. *Nat Gas Ind* 39(7):88–93

**Publisher's Note** Springer Nature remains neutral with regard to jurisdictional claims in published maps and institutional affiliations.

Springer Nature or its licensor (e.g. a society or other partner) holds exclusive rights to this article under a publishing agreement with the author(s) or other rightsholder(s); author self-archiving of the accepted manuscript version of this article is solely governed by the terms of such publishing agreement and applicable law.